

REJUVENATING & QUENCHING: GAS
PROPERTIES OF TRANSITIONAL
GALAXIES

REJUVENATING & QUENCHING: GAS PROPERTIES OF
TRANSITIONAL GALAXIES

By DYLAN LAZARUS, B.Sc.

A Thesis Submitted to the School of Graduate Studies in Partial
Fulfillment of the Requirements for
the Degree Master of Science

McMaster University © Copyright by Dylan Lazarus, December

2023

McMaster University

MASTER OF SCIENCE (2023)

Hamilton, Ontario, Canada (Physics and Astronomy)

TITLE: Rejuvenating & Quenching: Gas Properties of Transitional Galaxies

AUTHOR: Dylan Lazarus
B.Sc. (Physics),
McGill University, Montreal, Canada

SUPERVISOR: Laura Parker

NUMBER OF PAGES: ix, 96

Abstract

Most galaxies are either actively forming stars or quenched, but there is a small number of galaxies in transition from one population to the other. These galaxies are “quenching” if they are in the process of becoming quenched or “rejuvenating” if they are returning to the star-forming main sequence after a period of being quenched. Quenching occurs when a galaxy’s limited cold gas supply is heated or removed, halting star formation, while rejuvenation refers to any process that reintroduces cold gas to quenched galaxies, reigniting star formation. Rejuvenating galaxies, which are significantly rarer and less well-studied than quenching galaxies, can offer valuable insights into galaxy evolution processes. This thesis investigates the properties of transitional galaxies, with a focus on their gas content, to explore the mechanisms driving quenching and rejuvenation. We employ a recent classification method using GALEX NUV and Sloan Digital Sky Survey $H\alpha$ measurements to identify transitional galaxies and analyze the derived gas properties of those in the xGASS and xCOLD GASS surveys. We find that rejuvenating and quenching galaxies have intermediate gas fractions compared to actively star-forming and quenched galaxies, and that rejuvenating and quenching galaxies have similar depletion times to star-forming and quenched galaxies, respectively. We also find that the rejuvenating population, particularly at lower stellar mass, is efficient at converting its atomic gas supply to molecular hydrogen, which could be attributed to their high gas-phase metallicities at low stellar mass.

Acknowledgements

When I was five years old, my parents took me to the Hayden Planetarium in New York. At the end of the presentation, they encouraged me to ask the presenter, Neil DeGrasse Tyson, questions that I had about the universe. This brought out a curiosity that I have carried with me to this day.

Thank you, Mom, Dad, Brandon, and my confidant, Matthew, for always being a phone call or a six-hour drive away, and for always encouraging me and taking a genuine interest in my work. The same goes for you, Grandma, and I know Papa would have loved to have read this as well.

To all my friends at Mac, you have made my time here so enjoyable, and thank you for making me feel right at home. A special shout-out to Lauren and Hannah for the always-needed and welcomed coffee and gym breaks, and to Megan C., thank you for the office.

I also couldn't ask for a better research group in Megan O., Lauren, and Matías. Bouncing ideas off of all of you has played a huge part in shaping my research.

To my supervisor, Dr. Laura Parker, I would like to thank you so much for your guidance, knowledge, understanding, and boundless patience. These past two years have been such a rewarding and transformative experience, and I am really looking forward to working with you over the next four years.

And to Winslow, “woof”.

Table of Contents

| | |
|--|------------|
| Abstract | iii |
| Acknowledgements | iv |
| 1 Introduction | 1 |
| 1.1 Galaxy Properties | 1 |
| 1.1.1 Morphology | 2 |
| 1.1.2 Stellar Mass | 3 |
| 1.1.3 Star Formation Rate | 5 |
| 1.1.4 Active Galactic Nuclei | 9 |
| 1.1.5 Star-Forming Gas | 10 |
| 1.1.6 Derived Gas Properties | 11 |
| 1.1.7 Metallicity | 13 |
| 1.1.8 Dust | 15 |
| 1.2 Galaxy Evolution | 16 |
| 1.2.1 Quenching | 16 |
| 1.2.2 Rejuvenation | 19 |
| 1.3 Motivation & Outline | 20 |
| 2 Data and Methods | 22 |
| 2.1 Sample Selection | 22 |
| 2.1.1 SDSS | 22 |
| 2.1.2 The Cleland & McGee Method | 23 |
| 2.1.3 AGN Contamination | 27 |

| | | |
|----------|---|-----------|
| 2.1.4 | Dust Correction | 29 |
| 2.2 | Global Gas Measurements | 32 |
| 2.2.1 | HI Masses | 33 |
| 2.2.2 | H ₂ Masses | 36 |
| 2.2.3 | Derived Gas Properties | 40 |
| 2.2.4 | Statistical Methods | 40 |
| 3 | Results | 42 |
| 3.1 | Gas Fractions | 42 |
| 3.1.1 | ALFALFA | 42 |
| 3.1.2 | xGASS | 45 |
| 3.1.3 | xCOLD GASS | 49 |
| 3.1.4 | Total Gas | 52 |
| 3.2 | Derived Gas Properties | 55 |
| 3.2.1 | Depletion Time | 55 |
| 3.2.2 | Molecular-to-Atomic Gas Ratio | 60 |
| 3.3 | Gas Phase Metallicity | 63 |
| 3.3.1 | Full Sample | 63 |
| 3.3.2 | xCOLD GASS Sample | 69 |
| 3.4 | Dust Effects on the Rejuvenating Sample | 70 |
| 4 | Discussion & Future Work | 79 |

List of Figures

| | | |
|------|--|----|
| 1.1 | The Hubble Tuning Fork | 2 |
| 1.2 | SFR vs. Stellar Mass vs. Morphology | 7 |
| 1.3 | Gas-Phase Metallicity vs. Stellar Mass vs. SFR | 14 |
| 2.1 | Full SDSS DR7 Sample Stellar Mass vs. Redshift | 23 |
| 2.2 | Cut on SDSS DR7 $H\alpha$ Equivalent Width vs. Stellar Mass | 25 |
| 2.3 | Cut on NUV-Derived sSFR vs. Stellar Mass for GSWLC-A Sample | 26 |
| 2.4 | BPT Schematic with Rejuvenating and SDSS DR7 Parent Samples | 28 |
| 2.5 | $H\alpha$ to $H\beta$ Flux Ratio Distributions | 31 |
| 2.6 | Inclination Distributions for the Star-Forming and Rejuvenation Samples | 32 |
| 2.7 | HI Mass Fractions vs. Stellar Mass for the xGASS Representative Sample, ALFALFA-SDSS A100, and the Brown et al. (2015) Sample | 36 |
| 3.1 | ALFALFA HI Mass Fractions vs. Stellar Mass | 43 |
| 3.2 | HI Mass Fraction Residuals | 44 |
| 3.3 | xGASS HI Mass Fractions vs. Stellar Mass | 46 |
| 3.4 | HI Mass Fraction Residuals | 47 |
| 3.5 | xCOLD GASS H_2 Mass Fractions vs. Stellar Mass | 50 |
| 3.6 | H_2 Mass Fraction Residuals | 51 |
| 3.7 | Total Gas Mass Fractions vs. Stellar Mass | 53 |
| 3.8 | Total Gas Mass Fraction Residuals | 54 |
| 3.9 | H_2 Depletion Time vs. Stellar Mass | 56 |
| 3.10 | Total Gas Depletion Times vs. Stellar Mass | 58 |
| 3.11 | Total Gas Depletion Time Residuals | 59 |

| | | |
|------|--|----|
| 3.12 | Molecular-to-Atomic Gas Ratios vs. Stellar Mass | 61 |
| 3.13 | Molecular-to-Atomic Gas Ratio Residuals | 62 |
| 3.14 | O3N2-Derived Gas Phase Metallicity vs. Stellar Mass | 65 |
| 3.15 | MPA-JHU Gas-Phase Metallicity vs. Stellar Mass | 67 |
| 3.16 | SFR-Matched MPA-JHU Gas-Phase Metallicity vs. Stellar Mass | 68 |
| 3.17 | MPA-JHU Gas-Phase Metallicity vs. Stellar Mass for Galaxies in xCOLOD GASS | 70 |
| 3.18 | MPA-JHU Derived Gas Phase Metallicity vs. Stellar Mass for Galaxies with $0.025 < z < 0.05$ | 71 |
| 3.19 | Attenuation Factor KDE Distributions | 73 |
| 3.20 | Dust Corrected Total Gas Mass Fractions vs. Stellar Mass . . . | 75 |
| 3.21 | Dust Corrected Total Gas Depletion Times vs. Stellar Mass . . . | 76 |
| 3.22 | Dust Corrected Molecular-to-Atomic Gas Ratios vs. Stellar Mass | 77 |

List of Tables

| | | |
|-----|---|----|
| 2.1 | Rejuvenating Galaxies in Molecular Gas Surveys | 39 |
| 2.2 | Gas Survey Sample Sizes | 40 |
| 3.1 | HI Mass Fraction Statistical Test Results | 48 |
| 3.2 | H ₂ Mass Fraction Statistical Test Results | 51 |
| 3.3 | Total Gas Mass Fraction Statistical Test Results | 54 |
| 3.4 | Depletion Time Statistical Test Results | 60 |
| 3.5 | Molecular-to-Atomic Gas Ratio Statistical Test Results | 63 |
| 3.6 | Summary of Gas Properties of Rejuvenating Galaxy Sample | 78 |

Chapter 1

Introduction

The discovery of galaxies beyond the Milky Way, a groundbreaking revelation confirmed by Edwin Hubble a mere century ago, fundamentally transformed our understanding of the universe. This moment marked the beginning of a journey that has led to a rapidly growing knowledge about how galaxies evolve and the mechanisms driving their evolution. Although we currently have detailed models that depict the typical life cycle of galaxies across different environments and cosmic times, these models remain incomplete as they do not consider a galaxy's full breadth of evolutionary pathways. Using the large amounts of rich data available today, we can conduct detailed studies on outlier populations to further our understanding of galaxy evolution and refine our galaxy evolution models.

1.1 Galaxy Properties

Galaxies can vary widely in their characteristics, depending on their evolutionary stage, and interactions with their environment. To distinguish galaxy populations and describe their features and evolutionary pathways, we use properties that can be derived from observations. In the following sections, I discuss several galaxy properties that are particularly useful in the study of galaxy evolution.

1.1.1 Morphology

Galaxies can be subdivided into different classes based on their visual appearance. Most notably, the Hubble Sequence, created by Hubble (1926), divides galaxies into three morphological types: ellipticals, spirals, and irregulars, as shown on the Hubble Tuning Fork in Figure 1.1 from Hubble (1936).

Ellipticals, or ‘early-type’ galaxies, form the ‘handle’ of the tuning fork, making them ‘early’ in the sequence, not necessarily in their evolution. They are symmetric galaxies with smooth profiles, red in colour, and consist of older and more evolved stellar populations (Djorgovski & Davis, 1987; Kennicutt, 1998a; Kormendy et al., 2009). An E0 appears nearly spherical, with increasing values representing a more ellipsoidal geometry up to E7.

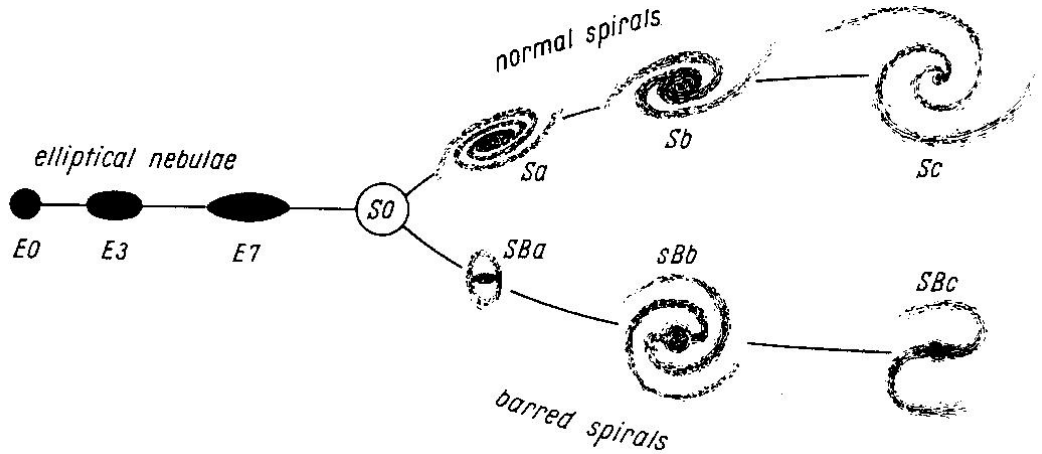


Figure 1.1: Edwin Hubble’s drawing of the famous “Hubble Tuning Fork” from Hubble (1936). Elliptical galaxies are on the left, from low to high ellipticity. Barred and unbarred spirals are on the prongs of the fork, with looser spiral arms from left to right.

Spirals, or ‘late-type’ galaxies, form the prongs of the tuning fork, making them ‘late’ in the sequence. They are bluer in colour than ellipticals, with

significantly higher mean star formation rates (Kennicutt, 1998a; Bell et al., 2003). Spirals have more complex morphologies, characteristically made up of a central bulge of old stars and a disk containing dust and gas-rich star-forming spiral arms (Freeman, 1970; Kennicutt, 1998a; Moorthy & Holtzman, 2006). Due to their complex and varied morphologies, they are subdivided into barred, SB, and non-barred, S, spirals, with additional classification based on how tightly wound the spiral arms are. Sa galaxies have tightly wound spiral arms, while Sc galaxies have loose spiral arms. An intermediate galaxy morphology is lenticulars, or S0, an example of ‘early-type’ galaxies with no apparent spiral arms but prominent bulges (Hubble, 1936).

Galaxy morphologies are often described using the bulge-to-total (B/T) parameter, which takes the ratio of the bulge luminosity and the disk luminosity. While susceptible to inclination biases, this can be beneficial over visual classification, as morphology can be described using a single parameter and computed automatically. Elliptical galaxies have a B/T of ~ 1 , while normal spiral galaxies have smaller bulge-to-totals, $\lesssim 0.3$ (Graham & Worley, 2008).

1.1.2 Stellar Mass

Many galaxy properties correlate with its mass, such as luminosity, colour, morphology, size, and mean stellar age (Conselice, 2006). Dark matter accounts for most of a galaxy’s total mass; for example, the Milky Way’s virial mass is estimated to be around $1.26 \times 10^{12} M_{\odot}$, while its stellar mass is only $2.4 \times 10^{10} M_{\odot}$ (McMillan, 2011). However, total mass is difficult to estimate since we cannot directly observe dark matter, and we need to rely on methods like rotation

curves or gravitational lensing. These methods require expensive and extensive observations and cannot be easily obtained for large samples of galaxies. Thus, we use the mass of a galaxy’s luminous matter, i.e. stars, as a proxy for its total mass. Measurements of galaxy mass-to-light ratios, the ratio of total galaxy mass to total luminosity, typically follow a tight correlation with luminosity (Faber & Gallagher, 1979). More recent work has more explicitly shown the tight relation of galaxy halo to stellar mass using weak gravitational lensing (Hudson et al., 2015). Therefore, stellar mass can be used instead of total mass when searching for relationships or inferring galaxy properties. Many of the galaxy properties focused on in this study show trends with stellar mass, including gas-phase metallicity and gas abundances, which are discussed later in this section.

A galaxy’s spectrum gives insight into its light-emitting matter. The spectrum includes radiation from stars, gas and dust heated by stars, and any emission generated by active galactic nuclei. Spectral energy distribution (SED) fitting routines (e.g. ProSpect, Robotham et al. (2020)) use broad/narrow band photometry covering a wide range of wavelengths to infer characteristics of a galaxy’s stellar population, including stellar mass, using pre-determined models of stellar population synthesis, dust attenuation, and nebular emission, among others. This method is advantageous over total mass estimation methods because the observations required are not as involved or costly as retrieving galaxy spectra; therefore, stellar masses can be estimated for large samples of galaxies in imaging surveys.

The stellar masses used in this study are from the GALEX-SDSS-WISE

Legacy Catalogue (GSWLC, Salim et al., 2016), which makes use of several wavelength bands in the ultraviolet (GALEX, Martin et al., 2005), optical (SDSS, Strauss et al., 2002), and infrared (WISE, Wright et al., 2010), described in more detail in Section 2.1.2. The GSWLC uses the Code Investigating GALaxy Emission (CIGALE, Noll et al., 2009) to estimate stellar mass, which works by constructing theoretical models of SEDs based on various parameters, including star formation history, stellar metallicity, and dust content. By comparing these models to the observed SEDs, CIGALE infers the most likely physical properties of the galaxies, notably stellar mass. Using data across a wide range of wavelengths reduces uncertainties when interpreting a galaxy’s SED. For example, SED fitting considers dust attenuation effects experienced by older stellar populations, where dust surrounding the stars absorbs their ultraviolet and optical radiation, making them appear less luminous than they truly are (Silva et al., 1998). The radiation absorbed by the dust is re-emitted in the infrared (Silva et al., 1998). Thus, the total luminosity of these stars can be estimated by including infrared data in the analysis. Therefore, more accurate stellar mass measurements can be made using a wide range of wavelengths, as done by SED fitting (Lower et al., 2020).

1.1.3 Star Formation Rate

Galaxy star formation rates (SFRs) are largely bimodal, with galaxies observed to be either rapidly forming stars and residing on the star-forming main sequence (SFMS) or quenched with low SFRs. Figure 1.2 from Cano-Díaz et al. (2019) shows the SFR versus stellar mass distribution for a sample of galaxies

in the SDSS-IV MaNGA survey (Bundy et al., 2015). Each panel shows the distribution for a different morphological type (late spirals, early spirals, lenticulars, and ellipticals), with blue points representing star-forming galaxies and red points representing passive galaxies. From this, we can see that late-type galaxies are mainly star-forming, with higher SFRs than early-type galaxies, which are primarily passive or quenched, with lower SFRs.

Galaxies undergoing strong star formation on the SFMS are characterized by bluer photometric signatures, indicating populations of young, massive stars (Evans et al., 2018). These galaxies also exhibit higher gas mass fractions (Saintonge et al., 2016) and are frequently characterized by disk-dominated morphologies (Kennicutt, 1998a). This contrasts the elliptical or spheroidal morphologies dominant among quenched galaxies. However, the distinction between galaxy populations is more apparent when using specific star formation rate (sSFR), which normalizes the SFR by the galaxy’s stellar mass. Galaxies on the SFMS have low stellar mass and high sSFR, and quenched galaxies typically have higher stellar masses and lower sSFRs (Peng et al., 2010).

UV as a Star Formation Tracer

The SFR of a galaxy is commonly measured using indicators that trace the presence of massive, short-lived stars. Ultraviolet (UV) radiation is a direct tracer of these stars, as these stars emit strongly in the UV before departing the main sequence. Stars that emit detectable thermal radiation in the UV are type O and B stars, with masses above $\sim 3M_{\odot}$ and lifespans on the order of 100Myr (Iben, 1967); therefore, using UV as a tracer for SFR allows us to peer into a

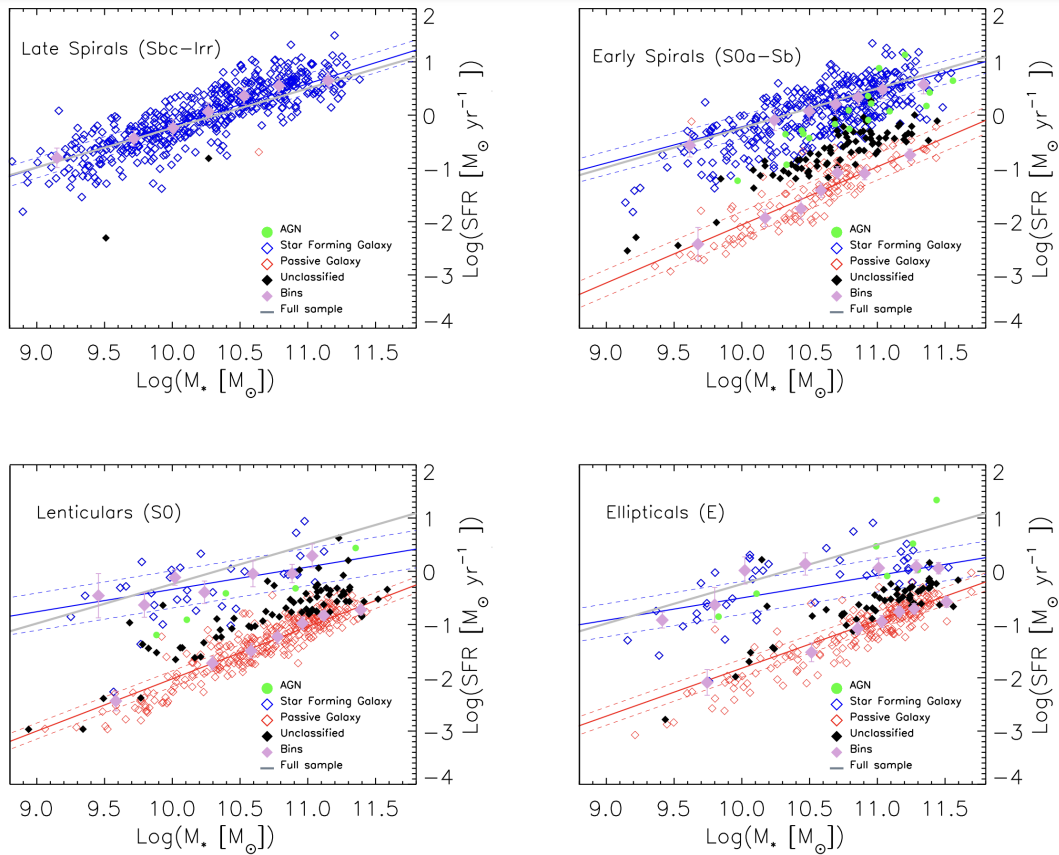


Figure 1.2: Figure 8 adapted from Cano-Díaz et al. (2019). SFR versus M_* plots for a sample ($N=1754$) from SDSS-IV ManGA. Each point represents a galaxy, coloured according to its star-formation classification. The pink points represent binned data used to compute a best-fit relation for the star-forming and quenched samples, shown with solid blue and red lines. The grey line shows the best fit to the full sample. The galaxies are divided by morphology, with late-type galaxies on the top row and early-type galaxies on the bottom.

galaxy’s evolution $\sim 100\text{Myr}$ ago. However, a caveat of this indicator is that UV light can be subject to absorption and scattering by interstellar dust (Silva et al., 1998). Ignoring dust effects, the UV-derived SFR is linearly correlated to a galaxy’s UV luminosity, with the equation given in Section 2.1.2.

H α as a Star Formation Tracer

H α is emitted by regions of ionized hydrogen gas (HII regions), typically found surrounding the most massive stars (spectral type O) born during active periods of star formation. These stars have masses $\gtrsim 8M_{\odot}$ and live up to approximately 10Myr (Meynet & Maeder, 2003; Weidner & Vink, 2010), allowing us to trace star formation on a shorter, approximately instantaneous timescale. This method benefits from being less affected by dust extinction than UV, but it still requires corrections for dust attenuation to accurately measure a galaxy’s intrinsic SFR. A galaxy’s H α -derived SFR is related to its H α luminosity using the following equation from (Kennicutt, 1998a),

$$\text{SFR}_{\text{H}\alpha} = 7.9 \times 10^{-42} L_{\text{H}\alpha} [\text{erg/s}]. \tag{1.1.1}$$

H α equivalent width (EW) compares the emission line to the continuum, which are both dust-affected. Thus, the EW measurement inherently partially accounts for dust effects. While the emission line is generally more attenuated than the continuum, EW is preferred over flux as it has negligible dust effects (Kashino et al., 2013; Puglisi et al., 2016). However, H α EW measurements are sensitive to emission from AGN, which can also ionize the ISM. I discuss removing galaxies contaminated by AGN emission in Section 2.1.3.

1.1.4 Active Galactic Nuclei

Active Galactic Nuclei (AGN), found in the core of $\sim 10\%$ of galaxies in the local universe (Zhang et al., 2021), are among the most energetic phenomena observed in the universe. They are powered by the accretion of material onto supermassive black holes (SMBHs), which reside in the center of most massive galaxies (Kormendy & Richstone, 1995; Kormendy & Ho, 2013). Observational evidence suggests that AGN activity is linked to various processes in galaxies, such as mergers and interactions that can funnel gas into the central regions, triggering AGN activity (Hopkins et al., 2008). The intense radiation from AGN can profoundly affect their host galaxies, often referred to as AGN feedback, which is discussed in Section 1.2.1.

Spectral observations of AGN show characteristic broad emission lines produced by fast-moving gas in the broad-line region (BLR) close to the SMBH and narrow emission lines produced by slower-moving gas in the narrow-line region (NLR) further from the SMBH (Antonucci, 1993). The BLR exhibits strong hydrogen Balmer lines, $H\alpha$ and $H\beta$, due to the high gravitational potential near the SMBH (Peterson, 2006). The NLR receives high energy radiation from the BLR and is low density, which promotes emission of the forbidden lines (OIII, NII, etc.) (Groves, 2007; Ludwig et al., 2012). The forbidden lines arise from high ionization levels but are not detectable experimentally as laboratory conditions are high-density, favouring energy loss via collisions over photon production (Carroll & Ostlie, 2017). A galaxy dominated by star formation rather than AGN does not have sufficient high energy radiation to excite the forbidden transitions and, therefore, will have low ratios of forbidden lines to hydrogen

Balmer lines. A galaxy dominated by AGN will influence the entire galaxy, including the galactic disk, while a galaxy with its radiation output dominated by AGN will only experience effects in the galaxy’s central regions surrounding the SMBH, and likely would be classified as a “Composite” galaxy (See Section 2.1.3).

1.1.5 Star-Forming Gas

A galaxy’s fuel for star formation lies in its cold gas reserves of predominantly atomic and molecular hydrogen. Neutral atomic hydrogen (HI) is smoothly distributed throughout and beyond the stellar disk, radially and azimuthally, in the galaxy’s thick disk. HI can be seen as the long-term fuel for star formation as, over time, dense regions can radiatively cool and form giant molecular clouds (GMCs). This process is facilitated by dust, which shields the hydrogen atoms from UV radiation that would otherwise prevent them from binding together (Silva et al., 1998). Dust also provides a catalyzing surface for hydrogen atoms to stabilize and bond (Wakelam et al., 2017). These GMCs are composed primarily of molecular hydrogen (H_2), the short-term fuel for star formation. H_2 regions of particularly high density can fragment and collapse when internal pressure and turbulence are insufficient to counteract its own gravity. The HI in the thick disk is constantly cooling while falling into the stellar disk, fueling H_2 formation and, subsequently, star formation (Putman et al., 2008).

1.1.6 Derived Gas Properties

Gas Fractions

Observing the HI, H₂, and total gas (HI + H₂) mass fractions of different populations of galaxies gives insight into the star formation potential. We define the gas fraction of a galaxy as the ratio of respective gas mass to stellar mass. Galaxies on the SFMS typically have high gas fractions, having yet to convert substantial amounts of gas into stars (McGaugh & de Blok, 1997; Tacconi et al., 2010). Conversely, quenched galaxies will have low gas fractions by losing their gas to stripping or exhausting their gas supply.

Depletion Time

The depletion time is typically defined as the ratio of the gas mass (H₂ and total gas in this work) to the galaxy’s star formation rate (SFR). It estimates the timescale over which a galaxy would consume all its gas at the current star formation rate, assuming no further gas is added to the system. Star-forming galaxies usually exhibit shorter depletion times, indicating efficient star formation and a higher gas consumption rate. In contrast, galaxies with longer depletion times, or a lower star formation efficiency, are often in a more quiescent phase of star formation, either due to a lack of sufficient gas or the presence of mechanisms inhibiting star formation. Along the SFMS, depletion time gradually increases with stellar mass (Saintonge et al., 2017) and is drastically longer for galaxies below the main sequence. The Kennicutt-Schmidt star formation law relates the star-forming gas mass surface density to the star formation rate

of a galaxy (Kennicutt, 1998b). Galaxies generally follow a tight relation, suggesting that to first order, a galaxy's star formation rate surface density relies on its gas surface density.

Molecular-to-Atomic Ratio

The molecular-to-atomic hydrogen mass ratio quantifies the efficiency of a galaxy at converting its long-term gas reservoir to short-term star-forming gas. A higher ratio suggests that a significant portion of the galaxy's atomic hydrogen has been converted into molecular hydrogen, indicating likely efficient star formation processes. Conversely, a lower ratio implies less efficient conversion, likely due to the heating of the ISM, preventing the condensation of HI to H₂. This can be affected by several galaxy properties, including the gas-phase metallicity and morphology. As mentioned in Sections 1.1.7 and 1.1.8, high gas-phase metallicities and, therefore, high dust content, promote the cooling and condensation of HI into H₂ (Omukai, 2000; Bromm et al., 2001). As well, morphological differences between galaxy populations can yield differing molecular-to-atomic gas ratios (Obreschkow & Rawlings, 2009). Galaxies that are more centrally concentrated, typically further to the left in Figure 1.1.1, will have deeper potential wells. These strong gravitational forces compress the gas in central regions of the galaxy, which can facilitate the condensation of HI to form H₂ (Carroll & Ostlie, 2017).

1.1.7 Metallicity

Stellar winds and supernovae inject the heavy elements produced in stars and supernovae into the ISM. As galaxies evolve, their metallicity should increase, though this is modulated by the influx of low metallicity gas via accretion or mergers (Balsara et al., 1994). A galaxy’s star formation history, chemical evolution, and interaction history with its environment all contribute to its gas-phase metallicity.

While star formation impacts the gas-phase metallicity of a galaxy, the gas-phase metallicity can conversely affect star formation. Metals can more efficiently cool gas through line cooling than hydrogen and helium. This cooling encourages the collapse of molecular clouds into new stars, creating a positive feedback loop as successive generations of star formation gradually increase the metal content of the galaxy. High gas-phase metallicity also promotes the creation of dust grains in the ISM, which facilitates the conversion of HI to H₂, discussed in Section 1.1.5.

Gas-phase metallicity is typically quantified by oxygen abundance in the ISM and is calculated using several calibrations based on emission lines. The details of the metrics we use to derive oxygen abundance are provided in Section 3.3.

The gas-phase metallicity of a galaxy is known to correlate with other galactic properties such as mass, luminosity, and morphology - a relationship encapsulated in the mass-metallicity relation (Tremonti et al., 2004). More massive galaxies, which have formed more stars over their histories, tend to have higher metallicities. This trend suggests that metallicity is both a consequence of and

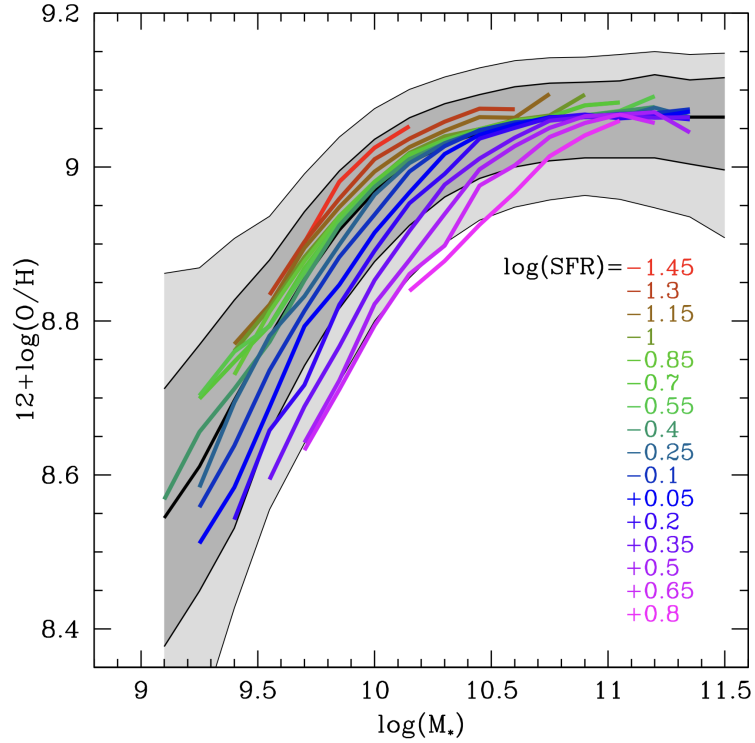


Figure 1.3: Figure 1 from (Mannucci et al., 2010), showing the gas-phase metallicity versus stellar mass, with the coloured curves representing varying star formation rates. Shows the general trend of higher gas-phase metallicity with higher stellar mass and lower gas-phase metallicity with higher global SFR.

a contributor to the star formation history of a galaxy (Tremonti et al., 2004). The mass-metallicity relation is shown in Figure 1.3 for local universe Sloan Digital Sky Survey (SDSS) galaxies from Mannucci et al. (2010), where we see a clear increase in oxygen abundance as stellar mass is increased. The colour gradient shows that star formation rate also correlates with a galaxy’s gas-phase metallicity, with higher global SFRs yielding lower metallicities. This trend with global SFR still holds with resolved SFR measurements (Baker et al., 2022).

1.1.8 Dust

Dust is a pervasive component of the interstellar medium (ISM), consisting primarily of silicate and carbonaceous particles ranging in size from a few nanometres to several microns (Williams, 2005). Dust grains originate in the cooler regions surrounding evolved stars and are ejected into the ISM through stellar winds or supernovae (Meyer & Zinner, 2006; Jones & Nuth, 2011), similar to the processes which increase the metallicity of the ISM. This ejection enriches the surrounding ISM with the building blocks for further dust formation and growth.

Dust grains absorb high-energy light and re-emit the energy in the infrared, shielding molecular gas from UV radiation from young stars (Silva et al., 1998). Dust's cooling and shielding effects can lead to the fragmentation of molecular clouds into smaller clumps, which can then individually collapse to form stars or star clusters. Also, shielding from UV helps shield H_2 from dissociation. As well, dust grains promote the formation of molecular hydrogen as discussed in Section 1.1.5.

Dust and metals in the ISM are typically correlated as their creation mechanisms are similar. However, galaxies have a lower dust-to-metal ratio at lower stellar mass and high sSFR, which can be explained partly by the intense UV field from intense star formation activity breaking apart dust grains (De Vis et al., 2019).

The effects of dust on the previously mentioned star formation tracers are discussed in Section 2.1.4.

1.2 Galaxy Evolution

From the moment a galaxy is born, it experiences many environmental and internal effects that can influence its properties and evolution. The life trajectory of a galaxy varies across populations in different environments and at different cosmic times, but typically, galaxies are born star-forming and evolve into quiescent and non-star-forming states. Various processes can drive galaxy quenching and have been well-studied across many environments. However, a small fraction of galaxies are reignited and experience star formation after having been quenched. This population, known as rejuvenating galaxies, is much less well-studied than quenching populations, and the mechanisms which drive rejuvenation have not been confirmed. In the following sections, we discuss the processes of galaxy quenching and candidate mechanisms driving rejuvenation at low redshift.

1.2.1 Quenching

As discussed in Section 1.1.3, galaxies are largely bimodal in SFR, dividing galaxies into either star-forming or quenched. Quenched galaxies are no longer strongly star-forming having evolved off of and below the SFMS. A galaxy will quench when it uses up or loses its supply of star-forming gas. There are many processes by which a galaxy can quench, driven by internal or environmental factors.

Major Mergers

Major merger events occur when a galaxy collides with another galaxy of similar mass ($M_1 \lesssim 3M_2$) (Stewart, 2009). These events can produce an initial burst of star formation in the merging galaxies, as the star-forming gas in the galaxies is compressed, forming over-dense regions susceptible to collapse (Lambas et al., 2012). However, these starbursts are short-lived and quickly use up the galaxies' star-forming gas reserve due to short depletion times. Major merger events occur more frequently in galaxy groups, where galaxies are moving more slowly and have time to experience a major interaction event (Conselice, 2021). These events also strongly affect galaxy morphology, as the merger of two spiral galaxies generally results in one massive, non-star-forming elliptical galaxy (Baldry et al., 2004).

Ram Pressure Stripping

A galaxy falling into a group or cluster experiences ram pressure from the intra-cluster medium (ICM). This pressure, which scales with the relative velocity of the galaxy through the ICM, exerts a force on the ISM. If this pressure exceeds the strength of gravity binding star-forming gas to the galaxy, it can remove this gas, halting star formation. Gas stripping is an outside-in mechanism, as gas on the outskirts of a galaxy is loosely bound and thus easier to strip (Schulz & Struck, 2001; Roediger & Hensler, 2005). As ram pressure stripping is an efficient process and typically occurs on first infall to the galaxy group or cluster, it has a short timescale of $\lesssim 1\text{Gyr}$ (Quilis et al., 2000).

AGN Feedback

AGN feedback can manifest as powerful particle jets releasing energy from material accreted onto the galaxy's central SMBH, radiatively/magnetically/thermally driven winds, or high energy radiation to the surrounding ISM. These mechanisms can heat the gas in the galactic halo, preventing the cooling of the star-forming regions of the ISM and potentially quenching star formation. AGN feedback-driven quenching occurs on timescales of $\sim 500\text{Myr}$ (Schawinski et al., 2007), being one of the fastest quenching mechanisms.

Tidal Interactions and Harassment

In dense environments such as galaxy clusters, galaxies are exposed to tidal interactions and brief high-speed encounters with other galaxies. These short-lived, high-energy interactions can cause disruptions in the galaxy's gas clouds, inducing temporary high star formation rates with low depletion times, which can quickly deplete a galaxy's gas reserve (Fujita, 1998; Moore et al., 1998). Tidal interactions can also remove star-forming gas from a galaxy, which can also cause rapid quenching (e.g. Spilker et al., 2022). The timescales for these processes are thus environmentally dependent and vary widely.

Starvation

Galaxy starvation occurs when a galaxy's long-term supply of star-forming gas is removed through various mechanisms, for example, ram pressure and tidal

interactions stripping the gas or the ICM heating the gas and preventing cooling. Since the galaxy’s long-term star-forming gas supply is ineffective at efficiently condensing into H_2 , it will gradually deplete its available short-term star-forming gas until star formation is naturally quenched. This is one of the longest quenching timescales, $\gtrsim 1\text{Gyr}$ (Peng et al., 2015; Trussler et al., 2020), as star formation halts slowly due to the less aggressive nature of starvation.

Morphological Quenching

As discussed in Section 1.1.1, galaxies tend to evolve from a spiral to elliptical morphology. Morphological quenching is the process by which gas in the disk of a spiral galaxy is stabilized against collapse through morphological transformations of the galaxy (Martig et al., 2009). Additionally, the formation of a galactic bar can drive gas inflows toward the centre of the galaxy, growing its bulge component (Wyse et al., 1997); the gas in bulge-dominated systems is more stable against collapse, creating unfavourable conditions for star formation. Morphological quenching occurs slowly, taking several Gyr to complete (Martig et al., 2009).

1.2.2 Rejuvenation

Galaxies typically evolve off the SFMS at a “transition mass” of $M_{\odot} \sim 10^{10.5} M_{*}$ (Kauffmann et al., 2003a) due to the processes mentioned above; however, there exists a small subset of galaxies that do not follow the typical evolutionary pathway. Quenched galaxies that evolve back onto the SFMS are classified as rejuvenating galaxies. Observationally, rejuvenating galaxy fractions seem to increase

as redshift decreases (Thomas et al., 2010; Akhshik et al., 2021). In simulations, the percentage of galaxies that have experienced a rejuvenation event throughout their lifetimes in the local universe is highly unconstrained, varying widely depending on the simulation, ranging from $\sim 10\%$ in IllustrisTNG (Nelson et al., 2018, 2019) to $\sim 70\%$ in UniverseMachine (Behroozi et al., 2019).

Any process that replenishes a galaxy’s cold gas supply or restores favourable conditions for star formation can induce a rejuvenation event. The mechanisms and timescales associated with rejuvenation are not well studied, though several candidate processes are outlined below.

Accretion of gas-rich dwarf galaxies or cold gas from the intergalactic medium can replenish a quenched galaxy’s star-forming gas supply. Accretion also increases the gas fraction of the quenched galaxy, creating conditions more suitable for star formation and inducing a rejuvenation event. Close encounters with neighbouring galaxies can also trigger rejuvenation by inducing gravitational perturbations, which could lead to gas inflows towards the galaxy centre (Ramón-Fox & Aceves, 2020). Finally, AGN feedback, as discussed as a quenching mechanism in Section 1.2.1, can potentially induce rejuvenation in a galaxy by compressing gas in the host galaxy, or by ejecting gas that eventually cools and falls back into the galaxy, replenishing its cold gas supply (Ishibashi & Fabian, 2012; Martín-Navarro et al., 2022)

1.3 Motivation & Outline

A novel method using multiple SFR indicators to identify rejuvenating galaxies is present in Cleland & McGee (2020), hereafter C&M; see Section 2.1.2 for

details. This work found that the rejuvenating fraction does not depend on environment. This hints that there is likely more than one dominant mechanism responsible for galaxy rejuvenation.

Outlier populations, like rejuvenating galaxies, are powerful constraints on galaxy evolution models, as any model of galaxy evolution must be able to reproduce both mean trends and the outlier populations we observe. As well, significantly more work has been done to understand the mechanisms driving galaxy quenching than rejuvenation.

This thesis uses the C&M method to identify rejuvenating and quenching samples to compare their atomic and molecular gas properties to regular star-forming galaxies and quenched galaxies. The gas properties of these galaxies can provide direct insight into possible mechanisms driving the rejuvenation.

In Chapter 2, I discuss the surveys and methods used to identify galaxies currently rejuvenating or quenching. I also present a potential modification to the Cleland & McGee method, considering dust effects, with our methodology presented in Section 2.1.4. Chapter 3 presents the results comparing the gas fractions, depletion times, molecular-to-atomic mass ratios, and gas-phase metallicities for the different galaxy populations. In Section 3.4, I present certain derived gas properties with the updated sample of rejuvenating galaxies, considering dust effects. In Chapter 4, I discuss the main results of this thesis, and present future work to expand on these results.

Chapter 2

Data and Methods

2.1 Sample Selection

2.1.1 SDSS

We use the Sloan Digital Sky Survey Data Release 7 (SDSS DR7) (Abazajian et al., 2009) as our starting sample for this study. SDSS DR7 contains nearly one million galaxies with global spectroscopic measurements with apertures covering the entire galaxy, and coverage of 9,380 square degrees of the sky up to a redshift of ~ 0.38 . SDSS is the largest survey of the local universe, allowing us to create a statistically significant parent sample of rejuvenating galaxies.

SDSS DR7 includes 5-band optical imaging and spectroscopy, and complementary catalogues of derived galaxy properties such as emission line measurements and galaxy colours are available (Kauffmann et al., 2003a; Brinchmann et al., 2004). In addition to the optical data from SDSS, there is complementary data at other wavelengths, including in the UV from GALEX (Salim et al., 2016) and IR from WISE (Wright et al., 2010).

We start with a sample of all 927,552 galaxies in SDSS DR7. To ensure relatively high completeness in our sample, we make a redshift cut at 0.1 and a stellar mass cut at $10^9 M_{\odot}$, commonly performed in the literature. This reduces bias towards brighter galaxies at higher redshift, as fainter galaxies are difficult to detect (Malmquist bias). The redshift cut of 0.1 also enables us to focus on

galaxies with short lookback times in the local universe. After making these cuts, we are left with a sample of 337,709 galaxies. We use spectroscopic redshifts from SDSS and stellar masses from GWLSC (Salim et al., 2016) calculated using multi-wavelength photometry from the UV to IR.

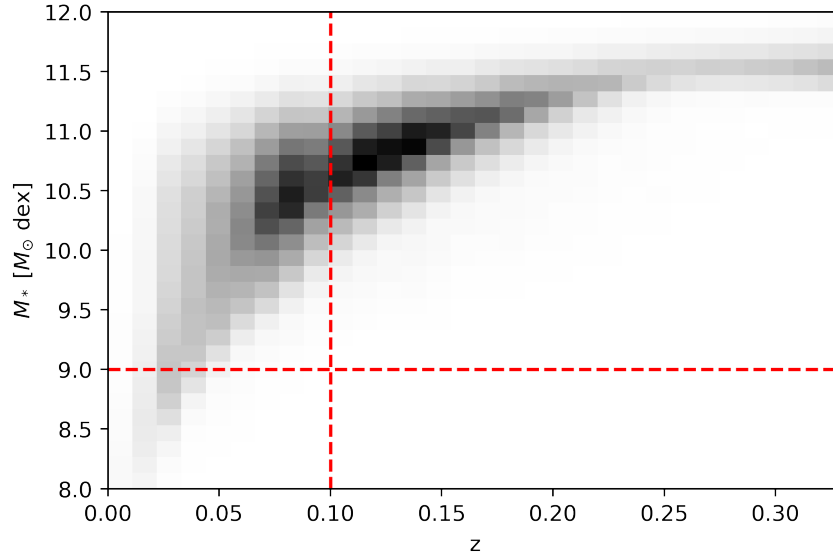


Figure 2.1: Stellar mass versus redshift for all SDSS DR7 galaxies. The vertical dashed line shows the redshift cut, where galaxies to the right of the line are removed from the sample. The horizontal dashed line shows the stellar mass cut, where galaxies below the line are removed from the sample.

2.1.2 The Cleland & McGee Method

This work builds on the methods and findings in Cleland & McGee (2020). They developed a simple framework to classify galaxies as currently rejuvenating or quenching using optical and UV star formation rate tracers. Their research centred on understanding how different environmental conditions influence these transitional galaxy populations.

As explained in Section 1.3, we are interested in comparing populations of galaxies undergoing episodes of rejuvenation and quenching. C&M found that galaxies currently undergoing rejuvenation, based on their selection method, exhibit no significant environmental dependence. This is a driving motivation for our work as it raises intriguing questions about the underlying mechanisms driving the rejuvenation of galaxies. We follow the selection method presented in C&M. This method uses $H\alpha$ and UV magnitudes, which trace star formation on 10^7 and 10^8 year time scales, respectively, as discussed in Section 1.1.3. This allows us to compare the star formation rates of a galaxy at different stages in its evolution. If a galaxy is star-forming in one tracer but not the other, we are observing it in a transitional phase.

The C&M method uses $H\alpha$ equivalent width (EW) measurements from SDSS DR7 and near-ultraviolet (NUV) magnitudes from the GALEX-SDSS-WISE Legacy Catalogue Medium-Deep Catalogue (GSWLC-M) as their star formation tracers. We also use $H\alpha$ EW measurements from SDSS DR7; however, we choose to use NUV magnitudes from the GSWLC All-Sky Catalogue (GSWLC-A). The All-Sky Catalogue GALEX measurements are not all of equal depth to the medium survey but cover many more galaxies. Our goal (see Section 1.3) is to determine the gas properties for as large a sample as possible, so we chose to use the all-sky version. This does not substantially impact our results as we only use this data for the selection process.

We use the specific star formation rate (sSFR) to classify a galaxy as star-forming or non-star-forming. Galaxy sSFRs are bimodal (Wetzel et al., 2012), allowing us to make a cut at the local minimum of the sSFR distributions in

$H\alpha$ and NUV. sSFRs above and below these cuts are defined as star-forming and non-star-forming, respectively. $H\alpha$ equivalent width is a direct and model-independent tracer of sSFR (Khostovan et al., 2021), so no conversion is necessary before performing the cut on the data. We convert NUV luminosity to SFR using an equation derived in Kennicutt (1998a),

$$\text{SFR}_{\text{UV}} = 1.4 \times 10^{-28} L_{\nu} [\text{erg s}^{-1} \text{Hz}^{-1}], \quad (2.1.1)$$

where L_{ν} is the luminosity at the peak NUV frequency. We then convert this to sSFR by normalizing by stellar mass. Figures 2.2 and 2.3 illustrate the cuts on the data used.

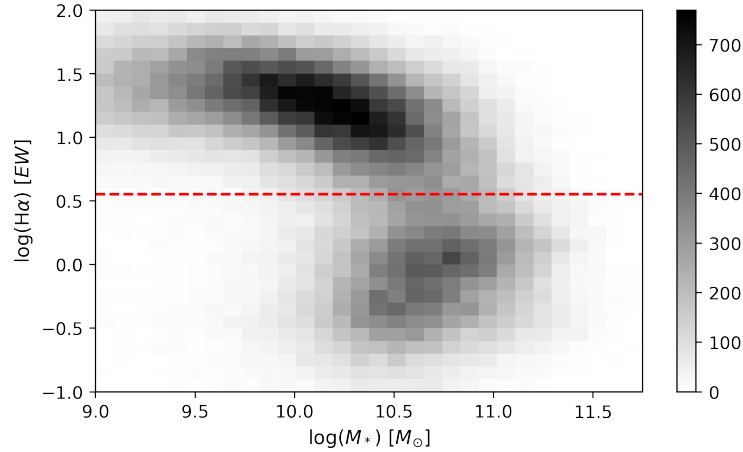


Figure 2.2: $H\alpha$ equivalent width versus stellar mass for galaxies in SDSS DR7 with $z < 0.1$ and $M_* > 10^9 M_{\odot}$. The dashed line represents the star-forming cut used on the data, where galaxies above the line are defined as star-forming in $H\alpha$.

We use $H\alpha$ EW as a direct tracer for specific star formation rate, as it compares the emission line to the continuum, and we do not convert these measurements to sSFRs. The cut we perform on $H\alpha$ EW is at the local minimum

of a Gaussian bimodal fit to the H α EW distribution of the total sample of stellar mass and redshift-selected SDSS DR7 galaxies. Galaxies above $H\alpha_{EW} = 3.5$ are classified as star-forming, as shown in Figure 2.2. For the UV sSFRs, again with a bimodal Gaussian, we fit to galaxies in GSWLC-M to extrapolate the cut between star-forming and non-star-forming, as it contains a more representative sample of galaxies than in GSWLC-A. The cut of $\log(\text{sSFR}_{UV}) = -11.1 \text{ yr}^{-1}$ is then applied to GSWLC-A NUV data as shown in Figure 2.3.

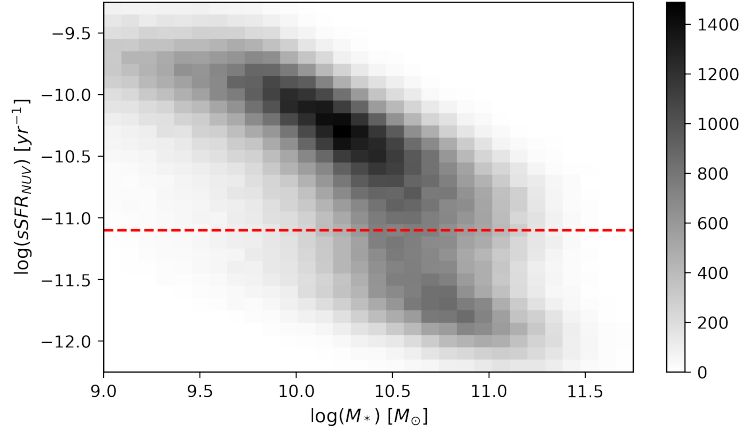


Figure 2.3: NUV-derived sSFR versus stellar mass for galaxies in the GSWLC-A sample with $z < 0.1$ and $M_* > 10^9 M_\odot$. The dashed line represents the star-forming cut used on the data, where galaxies above the line are defined as star-forming in NUV.

We define our galaxy populations as follows:

| | SF in UV? | SF in H- α ? |
|--------------|-----------|---------------------|
| Rejuvenating | | ✓ |
| Quenching | ✓ | |
| Star-Forming | ✓ | ✓ |
| Quenched | | |

If a galaxy is above our sSFR cut in H α and not in NUV, then the galaxy has experienced a rejuvenation event in the past $\lesssim 100\text{Myr}$. Similarly, if a galaxy

has recently shut off its star formation, it will be below our cut in $H\alpha$ and above in NUV, and classified as quenching.

After matching our SDSS data to that in the GSWLC-A, we are left with 230,944 galaxies with both $H\alpha$ and UV data, a lower sample size than previously due to galaxies having $H\alpha$ but no available UV measurements. Using the C&M selection method, we have samples of **16,347 rejuvenating**, **10,898 quenching**, **165,150 star-forming**, and **38,549 quenched** galaxies with optical spectroscopy, UV, and IR data from SDSS DR7, GALEX, and WISE respectively, with IR data only used for dust correction.

2.1.3 AGN Contamination

The $H\alpha$ emission observed in galaxies can originate from star formation and AGN activity. AGN can complicate the interpretation of $H\alpha$ emission, possibly categorizing such galaxies as actively star-forming. This is problematic, especially when they fall above our delineation, separating star-forming from quenched galaxies. To mitigate this, we filter out active galaxies from our sample of rejuvenating and star-forming galaxies, as both are defined by exceeding our $H\alpha$ equivalent width threshold.

The BPT (Baldwin-Phillips-Terlevich) (Baldwin et al., 1981) plot provides a means to distinguish between emission due to star formation and AGN activity. Within the BPT framework, different authors have derived various demarcation lines that classify galaxies based on their dominant emission source. We use a BPT plot most widely used in recent literature with emission line ratios $[OIII]/H\beta$ versus $[NII]/H\alpha$.

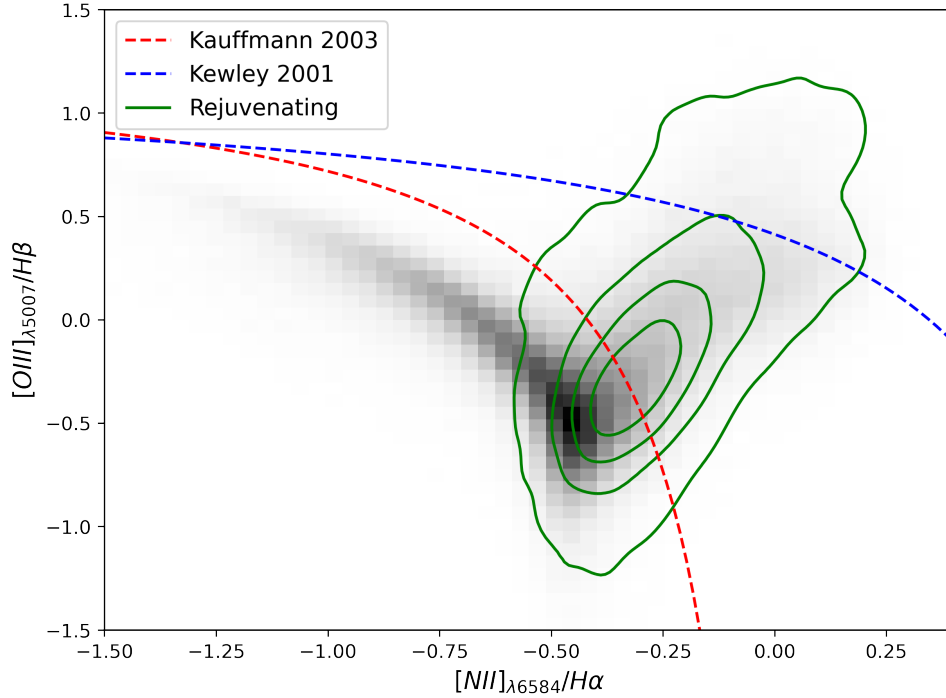


Figure 2.4: A BPT diagram of our parent sample of SDSS galaxies with $z < 0.1$ and $M_* > 10^9 M_\odot$. The K03 and Ke01 demarcation lines are overlaid. Rejuvenating parent sample contours are plotted in green ($N=16,347$). Galaxies selected as rejuvenating are removed from the sample if above the K03 line.

Kewley 2001 Line (Ke01): The Kewley et al. (2001) line represents a theoretical maximum starburst line, where galaxies lying above this line have emission primarily originating from AGN activity. The model used for this demarcation line was based on a mixture of photoionization by young stars and shocks to distinguish extreme starbursts from AGN. Galaxies above this line are subjected to a radiation field most likely governed by an AGN.

$$\log([\text{OIII}]/\text{H}\beta) = 1.19 + 0.61/[\log([\text{NII}]/\text{H}\alpha) - 0.47] \quad (2.1.2)$$

Kauffmann 2003 Line (K03): The demarcation presented in Kauffmann et al. (2003b) empirically separates star-forming galaxies from those hosting AGN. This line is derived from SDSS data, and star-formation processes primarily govern galaxies located below this line.

$$\log([\text{OIII}]/\text{H}\beta) = 1.3 + 0.61/[\log([\text{NII}]/\text{H}\alpha) - 0.05] \quad (2.1.3)$$

Those between the K03 and the Ke01 lines are classified as Composite galaxies, where both star formation and AGN processes contribute to their emission.

A typical signature of galaxies hosting AGN is a comparatively higher $\text{H}\alpha$ flux to UV flux. Due to our selection method, this is prevalent in our sample of rejuvenating galaxies. Approximately one-third of the galaxies in this sample are dominated by star formation, not AGN, as shown in Figure 2.4. After filtering out AGN, we are left with **5,075 rejuvenating galaxies** and **130,501 star-forming galaxies**.

2.1.4 Dust Correction

Emission from hot stars has the potential to be significantly attenuated by interstellar dust. Dust absorbs high-energy photons and re-emits them in the infrared, and the more energetic the light, the more attenuated it will be. Therefore, high dust concentrations in the ISM can impact the high-energy UV light from hot stars. On average, the UV star formation measurements used in this work are higher than measured, with the rejuvenating galaxy sample being particularly susceptible to dust effects due to our selection method. Meanwhile,

$H\alpha$ equivalent width measurements are quite robust against dust attenuation (Kashino et al., 2013; Puglisi et al., 2016), so we choose not to account for this in our data presented in Chapter 3.

Without accounting for dust effects on our data, a significant proportion of our sample of rejuvenating galaxies could be dusty star-forming galaxies in disguise. A dusty and star-forming galaxy would attenuate UV with greater intensity than $H\alpha$ in the optical, so we would classify the galaxy as non-star-forming in UV and star-forming in $H\alpha$. The differential effects of dust on UV versus $H\alpha$ were not considered in C&M. In Chapter 3, we present results using the original selection method but also explore the impact of dust in Section 3.4.

A simple spectroscopic measure of the dust content in a galaxy is the Balmer Decrement, which is the ratio of the $H\alpha$ and $H\beta$ flux. This quantifies the difference in dust attenuation between the higher energy $H\beta$ line and the lower energy $H\alpha$ line. Both emission line measurements are available in SDSS DR7.

In Figure 2.5, we show that the rejuvenating sample has the highest Balmer decrement on average compared to the quenched, quenching, and star-forming galaxy populations, which is partly attributed to a misclassification of the rejuvenating sample, or that truly rejuvenating galaxies are, on average, dustier than SFMS galaxies. The quenched and quenching galaxy populations are observed to have lower Balmer decrements than those of star-forming and rejuvenating, however, we cannot draw any robust conclusions from these samples as most of their galaxies have poor SNR in both emission lines. Since we require $\text{SNR} > 3$ for both emission lines, this samples the brightest galaxies within these two populations, typically more similar to star-forming galaxies.

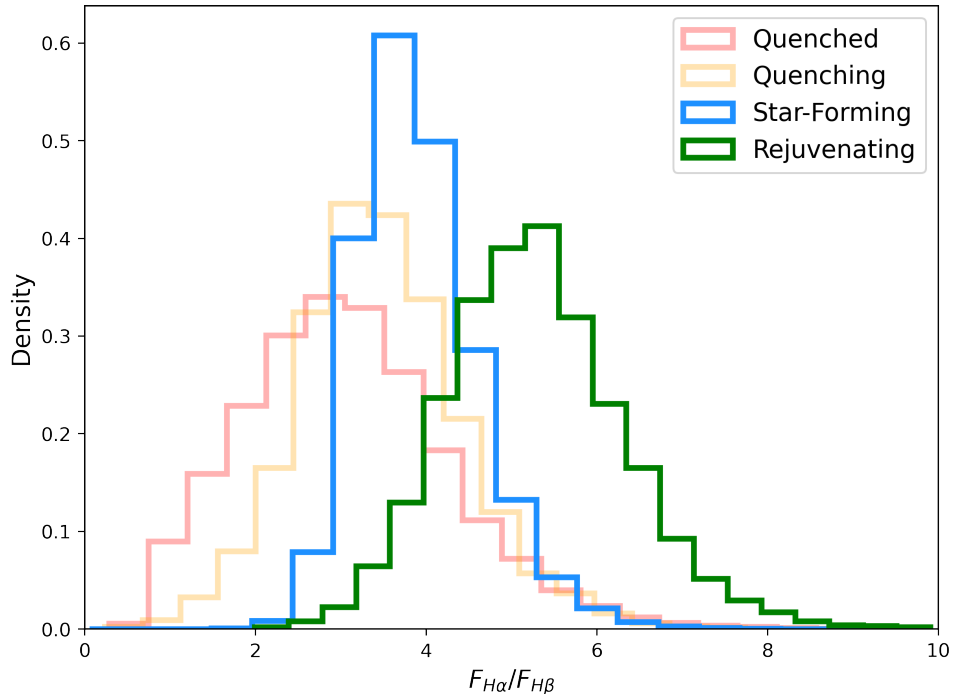


Figure 2.5: The $H\alpha$ to $H\beta$ flux ratio of the four sub-populations are compared here, with the areas under each curve equal to 1, where quenched and quenching galaxies have a lower ratio than star-forming, and rejuvenating galaxies have a higher flux ratio. This is a signature of more intense dust effects on the rejuvenating galaxy sample.

Along with a higher dust content, a galaxy’s inclination can also play a role in attenuating UV. We use Sersic minor (b) to major (a) axis measurements from the NASA Sloan Atlas (NSA) catalogue (Blanton et al., 2011a), which covers the majority of SDSS DR7. Sersic model fitting is performed on SDSS optical images (Blanton et al., 2011b), where the inclination of the galaxy, assuming a circular stellar disk, is calculated with $i = \arccos(b/a)$.

The rejuvenating population has a median inclination of 69.9° compared to the star-forming population’s 55.5° . Using the Kolmogorov-Smirnoff (KS) test, we see that the distributions of both samples are statistically different.

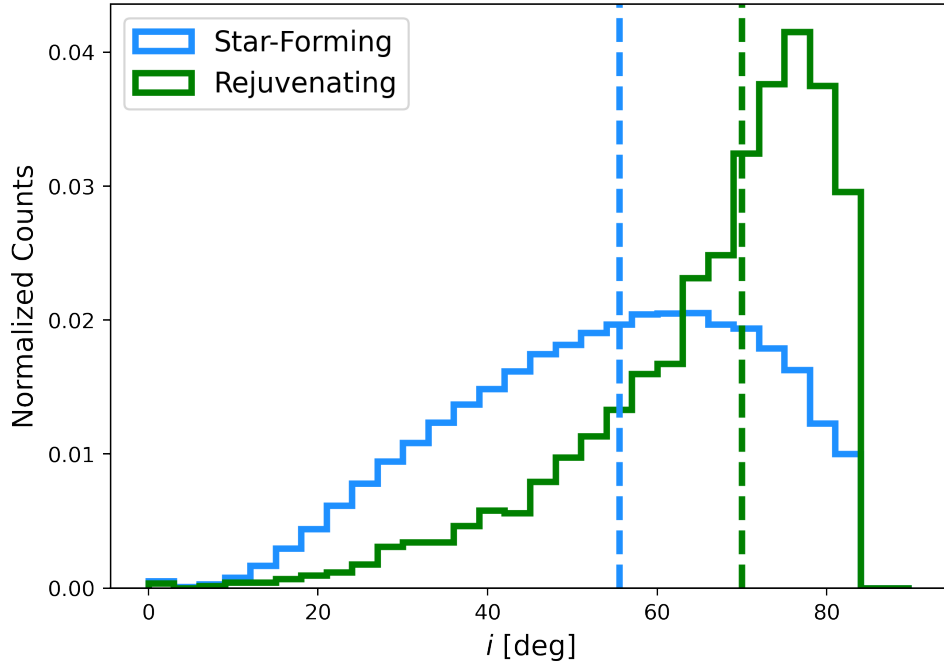


Figure 2.6: Inclinations calculated from Sersic fits to SDSS DR7 optical images of the rejuvenating and star-forming populations. Dashed lines show the median of each population. On average, the rejuvenating population has a higher inclination than star-forming galaxies.

The selection method for rejuvenating galaxies presents significant bias towards galaxies at high inclinations, which also motivates correcting UV for dust attenuation.

2.2 Global Gas Measurements

Observing the gas content of a galaxy provides information on its long and short-term fuel for star formation. Both atomic (HI) and molecular (H_2) hydrogen can provide significant insight into the mechanisms that can trigger either rejuvenation or rapid quenching. However, as gas surveys are challenging and

costly, limited data is available for many galaxies in our sample. Thus, to maintain a large sample size of galaxies with gas measurements, we neglect the effects of dust attenuation on our NUV SFRs.

We match our final parent samples of transitional galaxies and control populations as defined by the C&M selection method to multiple surveys with measurements of HI and H₂, as discussed in Sections 2.2.1 and 2.2.2. There are only small samples of galaxies with atomic and molecular global gas measurements, with even smaller samples with resolved gas measurements. Thus, this study uses global gas measurements to maintain large sample sizes.

2.2.1 HI Masses

A galaxy's HI mass can be derived from its HI line profile. Frequencies around the 21 cm line can be converted to velocities, in which the flux is integrated over, to obtain the total flux of the 21 cm line (Giovanelli et al., 2005). In the ideal case, velocity profiles are double-horned, primarily caused by the galaxy's rotation, as well as secondary small-scale deviations from the overall motion of the gas. The integrated 21cm flux can be approximated by using the peak flux S_{peak} in Janskys and the velocity width W in km/s. The HI gas mass can then be calculated by,

$$M_{HI} \approx 2.4 \times 10^5 M_{\odot} D_{Mpc}^2 S_{peak} W_{kms^{-1}}, \quad (2.2.1)$$

where D_{Mpc} is the distance to the galaxy in Mpc (Giovanelli et al., 2005). Note that this method assumes that the HI gas is optically thin, which is generally valid for diffuse HI gas but may be subject to limitations if the gas is highly

concentrated or if there are complexities in the velocity field that are not resolved by the observations (i.e., mergers and interactions).

ALFALFA:

The Arecibo Legacy Fast ALFA (ALFALFA) survey (Durbala et al., 2020) benefits our study due to its large $\sim 30,000$ galaxy sample. ALFALFA galaxies are HI-selected and thus biased towards galaxies with high gas masses. However, comparing the HI properties of all four galaxy populations will still provide valuable insight into the HI content of the transitional galaxy populations. A strict signal-to-noise cut of > 6.5 is applied to SDSS-matched ALFALFA measurements to remove galaxies with poor HI readings. This leads to over 80 percent of ALFALFA galaxy targets being non-detections and excluded from publicly available data products. This could significantly affect the completeness of our non-star-forming populations, in particular, by leaving galaxies with low gas mass unaccounted for. A significant portion of ALFALFA galaxies have HI masses above $10^8 M_\odot$, with a small percentage between $10^7 M_\odot$ and $10^8 M_\odot$, and galaxies between $10^6 M_\odot$ and $10^7 M_\odot$ can only be detected out to a redshift of 0.0015 (Giovanelli et al., 2005). Galaxies in ALFALFA characteristically have bluer colours and lower stellar masses, typical for galaxies with high gas content (Huang et al., 2012).

xGASS:

The Extended GALEX Arecibo SDSS Survey (xGASS) is a combination of GASS and GASS-low (Catinella et al., 2010, 2018), providing HI masses for

~ 1200 galaxies in a redshift range of $0.025 < z < 0.05$. Unlike the ALFALFA survey, it does not select sources based on HI detection. Instead, the galaxies in xGASS are randomly selected based on redshift and stellar mass for galaxies with complementary GALEX data to create a significantly more unbiased sample than ALFALFA. The stellar masses in GASS range from $10^{10} M_{\odot}$ to $10^{11.5} M_{\odot}$, designed to sample galaxies at the typical stellar masses spanning across the “transition mass” of $10^{10.5} M_{\odot}$ (Kauffmann et al., 2003a). Since galaxies in GASS have higher stellar masses, lower stellar masses were later added to the sample in GASS-low to extend the stellar mass range to $10^9 M_{\odot}$. An HI gas mass fraction lower limit of $M_{HI}/M_* > 0.01$ is applied to xGASS galaxies with stellar masses below $10^{10.5} M_{\odot}$ to optimize their observation time and small sample size. This can leave us with a partially incomplete sample of quenched galaxies, as gas mass fractions this low are typical for early-type galaxies.

xGASS Representative Sample:

The catalogue used in this research is called the “xGASS Representative Sample.” It consists of galaxies from xGASS and stellar mass/redshift-selected galaxies from the gas-rich ALFALFA and the HI Cornell Archive (Springob et al., 2005). This combination provides a more realistic sample than any of the surveys on their own.

In Figure 2.7, we show HI mass fractions for the xGASS Representative Sample and the SDSS-matched ALFALFA sample, compared to a stacked HI sample from previous work by Brown et al. (2015). In Brown’s work, stacking is performed on a selected sample of ALFALFA non-detections to significantly

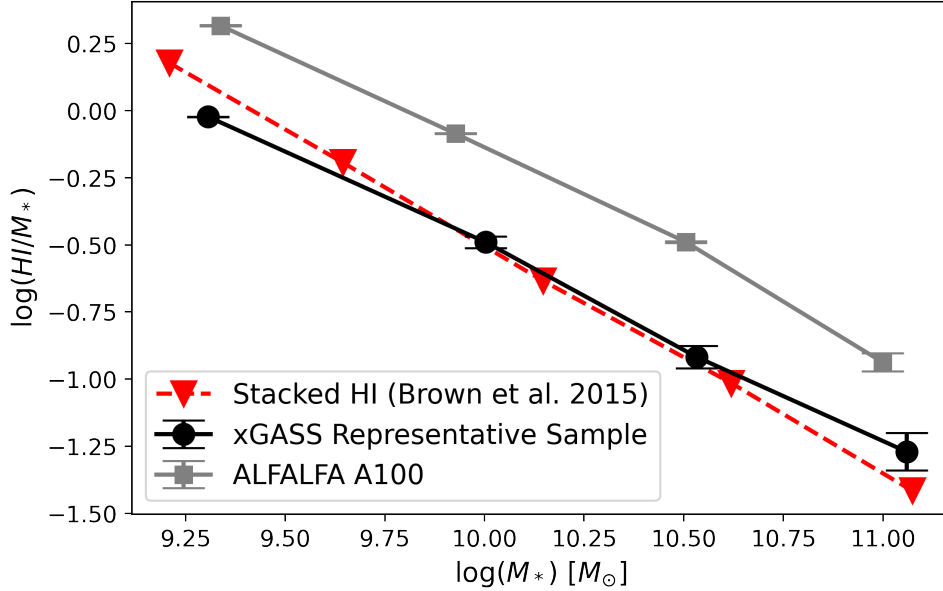


Figure 2.7: HI mass fractions from the xGASS Representative Sample, ALFALFA-SDSS A100, and the stacked galaxy sample from Brown et al. (2015) are compared. Bin values are calculated through the logarithm of the means of the binned samples in both HI mass fraction and stellar mass. Error bars are the standard error in each bin.

reduce noise in the HI spectra. This produces an effectively unbiased look at the HI content of galaxies in the local universe and a means to compare the two catalogues we use for our analysis. We can see that the ALFALFA galaxies are HI-rich at all stellar mass bins, while xGASS is nearly unbiased. Though xGASS has a significantly smaller population of galaxies than ALFALFA (1,179 vs. 31,501), we can more robustly compare our four galaxy populations.

2.2.2 H_2 Masses

Molecular hydrogen (H_2) in galaxies is predominantly found at low temperatures ranging between $\sim 10 - 20K$, while only emitting detectable radiation

at much higher temperatures ($\gtrsim 500\text{K}$). This contrast in temperature ranges poses a significant challenge for directly measuring H_2 abundances in extragalactic sources. We can use tracer molecules to circumvent this issue to infer H_2 abundances. In recent molecular gas surveys of the local universe (Saintonge et al., 2018; Brown et al., 2021), emission lines from specific energy transitions of the carbon monoxide (CO) molecule have proven to be a reliable tool for this purpose.

Historically, a constant CO-to- H_2 conversion factor, derived from observations within the Milky Way, has been used (Narayanan & Hopkins, 2013). This assumes that the physical conditions influencing the relationship between CO and H_2 are uniform across different regions of a galaxy and all galaxy populations. However, studies have shown that this assumption is erroneous (Wilson, 1995; Israel, 2000), as the gas-phase metallicity, along with other factors such as gas density and temperature, affect the abundance of CO as compared to the abundance of H_2 in the ISM. Gas-phase metallicity is correlated with dust content, and dust shields the CO molecule from photodissociation. Therefore, if a constant CO-to- H_2 conversion factor is used, a low metallicity would underestimate the H_2 abundance.

We use H_2 masses from xCOLD GASS (Saintonge et al., 2017), as described in the section below, which applies a metallicity-dependent conversion factor to the CO(1-0) luminosities,

$$L_{\text{CO}1-0} = 3.25 \times 10^7 S_{\text{CO}1-0} \nu^{-2} D_L^2 (1+z)^{-3}, \quad (2.2.2)$$

where $S_{CO_{1-0}}$ is the total integrated flux of the CO(1-0) line and D_L is the luminosity distance. The CO(1-0) luminosity is then converted to an H_2 mass using the relationship $M_{H_2} = \alpha_{CO} L_{CO_{1-0}}$, where α_{CO} is the metallicity-dependant CO-to- H_2 conversion factor as calculated using the methodology presented in Accurso et al. (2017).

xCOLD GASS:

xCOLD GASS is a galaxy survey providing CO(1-0) derived H_2 masses for 532 galaxies with data gathered by the IRAM 30-metre telescope. This survey builds on the lower stellar mass end of COLD GASS (Saintonge et al., 2011), as was done for xGASS, where a constant CO-to- H_2 conversion factor was used but has since been updated to use a metallicity-dependent conversion factor. Galaxies in xCOLD GASS are randomly selected by stellar mass from xGASS to preserve the unbiased nature of the survey. Therefore, the stellar mass and redshift ranges of $10^9 < M_* < 10^{11.5} M_\odot$ and $0.025 < z < 0.05$ remain similar. Of the 532 galaxies in the sample, there are 199 non-detections, for which we are provided theoretical upper limits on H_2 masses as inferred from stacking, using a similar method to Brown et al. (2015).

Rejuvenating Galaxies in H_2 Surveys:

It is important that we use a molecular gas survey with a statistically significant number of rejuvenating galaxies within its sample, which is why we turn to xCOLD GASS. To gain more insight into the molecular gas content for rejuvenating galaxies, we explore the occurrences in other H_2 surveys. Below are the

number of rejuvenating galaxies within each of the eight molecular gas surveys we matched to.

| Survey | Rejuvenating Population |
|---------------------------------------|-------------------------|
| xCOLD GASS (Saintonge et al., 2017) | 19/532 |
| JINGLE (Saintonge et al., 2018) | 5/193 |
| EDGE-CALIFA (Bolatto et al., 2017) | 3/126 |
| VERTICO (Brown et al., 2021) | 0/51 |
| HERACLES (Leroy et al., 2009) | 0/48 |
| EMPIRE (Jiménez-Donaire et al., 2019) | 0/9 |
| FORNAX (Zabel et al., 2019) | 0/30 |
| PHANGS (Schinnerer et al., 2019) | 0/74 |

Table 2.1: Presence of rejuvenating galaxies using our selection method in various molecular gas surveys of the local universe. The fractions show the number of rejuvenating galaxies compared to the full survey sample.

We can see that xCOLD GASS contains the most rejuvenating galaxies, followed by JINGLE and EDGE-CALIFA. We choose not to include the five JINGLE rejuvenating galaxies in our analysis because H₂ masses are derived differently than in xCOLD GASS, with H₂ masses derived from the CO(2-1) line as opposed to the CO(1-0) line. As well, JINGLE uses the methodology presented in Sargent et al. (2014) to compute α_{CO} whereas xCOLD GASS follows that in Accurso et al. (2017). EDGE-CALIFA is a resolved molecular gas survey and, therefore, is not directly comparable to the global measurements of xCOLD GASS. xCOLD GASS, JINGLE, and EDGE-CALIFA all have similar fractions of rejuvenating galaxies in their samples.

The following table shows the final gas samples of our four sub-populations used for analysis in the following section.

| | ALFALFA | xGASS | xCOLD GASS |
|--------------|---------|-------|------------|
| Rejuvenating | 96 | 39 | 19 |
| Quenching | 644 | 54 | 20 |
| Star-Forming | 10,347 | 376 | 197 |
| Quenched | 331 | 330 | 140 |

Table 2.2: Number of galaxies in each population in each gas survey used in this study.

2.2.3 Derived Gas Properties

Combining HI and H₂ data from xGASS and xCOLD GASS allows us to study the interplay between different gas phases and the total gas available for star formation in our galaxy sub-populations. In particular, we observe the gas mass fractions derived from atomic and molecular hydrogen (M_{gas}/M_*), molecular ($M_{\text{mol}}/\text{SFR}$) and total gas depletion times ($M_{\text{gas}}/\text{SFR}$), and the molecular-to-atomic gas ratio (H₂/HI). These results are presented in the following chapter for the full sub-populations and later in Section 3.4 for the UV dust-corrected sub-populations.

2.2.4 Statistical Methods

We use several statistical tests to compare our galaxy population distributions in the following section, including the Kolmogorov-Smirnov (KS) test, the Anderson Darling (AD) test, and the Earth Mover’s Distance (EMD).

The two-sample KS and AD tests have similar applications, testing the null hypothesis that the samples are drawn from a different underlying distribution.

However, the AD test handles small sample sizes better and gives more importance to the tails of the distributions than the KS test. While the KS test is widely used, we use the AD test for most of our data due to the small sample sizes of our transitional galaxy populations.

The EMD tells us the “distance” between two distributions - i.e. the amount of “Earth” that has to be moved to transform one distribution into another. A lower EMD value indicates that the distributions are similar in shape and offset. By comparing the EMD of our transitional galaxy populations to each control population, we can infer whether the population is more similar to the star-forming or quenched distributions.

Chapter 3

Results

This section presents the gas properties of galaxies currently undergoing rejuvenation or a rapid quenching event. We compare our gas properties to the two control populations, star-forming and quenched galaxies.

Section 3.1 presents atomic hydrogen gas mass fractions from ALFALFA and xGASS, and molecular hydrogen gas mass fractions from xCOLD GASS. In Section 3.2, we present several derived gas properties, such as depletion time and molecular-to-atomic gas ratio. In Section 3.3, we examine the gas-phase metallicities of the sample. Finally, in Section 3.4, we take dust attenuation in the ultraviolet into account and present select findings with this improved methodology.

3.1 Gas Fractions

3.1.1 ALFALFA

The final ALFALFA 100% catalogue contains >30,000 HI-detected galaxies. In Figure 3.1, we show the HI mass fractions of our four galaxy populations with HI detections in the ALFALFA 100% catalogue. The histograms in Figure 3.1 show the distributions of stellar mass and HI mass fractions of each population. The populations matched to ALFALFA show that the star-forming

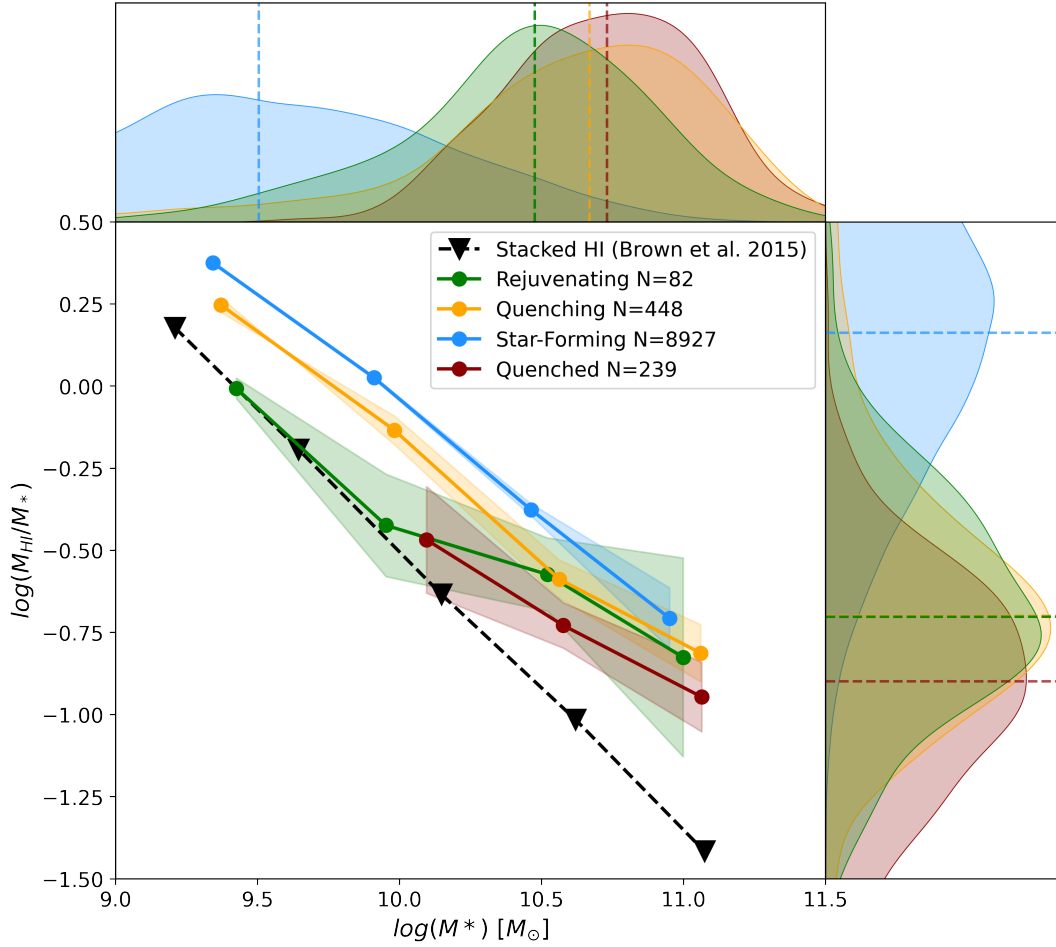


Figure 3.1: HI gas mass fraction versus stellar mass for the ALFALFA A100 sample. Stellar mass and HI mass fraction KDE distributions are shown above and to the right of the main plot. The dashed lines on the marginal distributions represent the median value of each population. Rejuvenating, quenching, star-forming, and quenched galaxies are coloured green, yellow, blue, and red, respectively. The data for each population is binned by stellar mass, with the data points representing the log of the means of the stellar mass and HI mass fraction. The shaded regions are the standard errors on the HI mass fraction means. The stacked HI mass fractions from Brown et al. (2015) are plotted in black as a representative galaxy population.

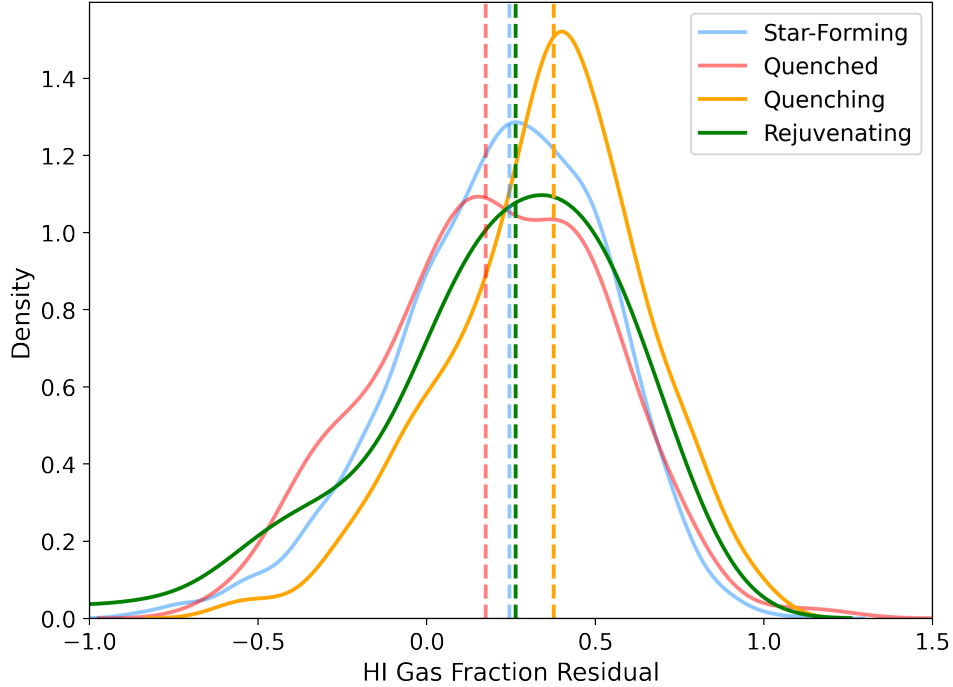


Figure 3.2: The HI mass fraction residuals to an OLS fit to the Brown et al. (2015) ALFALFA stacked galaxy sample. The area under each curve equals 1. The same colours are used for the four galaxy populations as in the previous figure. Medians of each distribution are plotted as dashed lines. The distributions are smoothed using KDEs.

galaxies occupy the low stellar mass end of the dataset. In contrast, the transitional and quenched populations sample the high stellar mass end. Each galaxy population in the main plot shows higher gas mass fractions than the Brown et al. (2015) stacked ALFALFA sample at all stellar masses. This indicates that the ALFALFA sample is biased towards galaxies with high HI abundances and preferentially samples the high gas mass end of particularly the quenched and quenching populations, as a lower fraction of these samples are gas-rich. This is expected because the galaxies in the ALFALFA sample are HI-selected. The discrepancies observed in the HI mass fraction distributions between populations

are attributed to first-order stellar mass effects.

In Figure 3.2, we show the residuals of the four galaxy populations to the ordinary least squares fit to the Brown et al. (2015) stacked galaxy sample. The medians of each galaxy population lie above zero, and none of the distributions are significantly different. Using a KS test, we confirmed that the residual distributions of the quenched and star-forming samples are not statistically different distributions, in contrast to the fact that galaxies on the star-forming main sequence have higher abundances of gas than galaxies below the main sequence. This is because ALFALFA contains only high signal-to-noise galaxies, leading to an incomplete sample of quenched galaxies. Thus, as shown by the residuals, these are not representative galaxy samples, and we cannot draw statistically significant conclusions from comparing transitional to control galaxy populations using the ALFALFA sample.

3.1.2 xGASS

We obtain HI mass fractions for our sample as described in Section 2.2.1 and show the HI mass fraction against stellar mass for the xGASS Representative Sample in Figure 3.3. We fit the star-forming and quenched populations using the Ordinary Least Squares (OLS) fitting function in the python package `statsmodels`. This fit does not consider error bars as we include upper limits. These fits and their errors are given by the dashed lines and the shaded regions. As expected, the star-forming and quenched populations are distinct, with the star-forming population having consistently higher atomic gas mass fractions across all stellar masses. A significant fraction, 55%, of the quenched

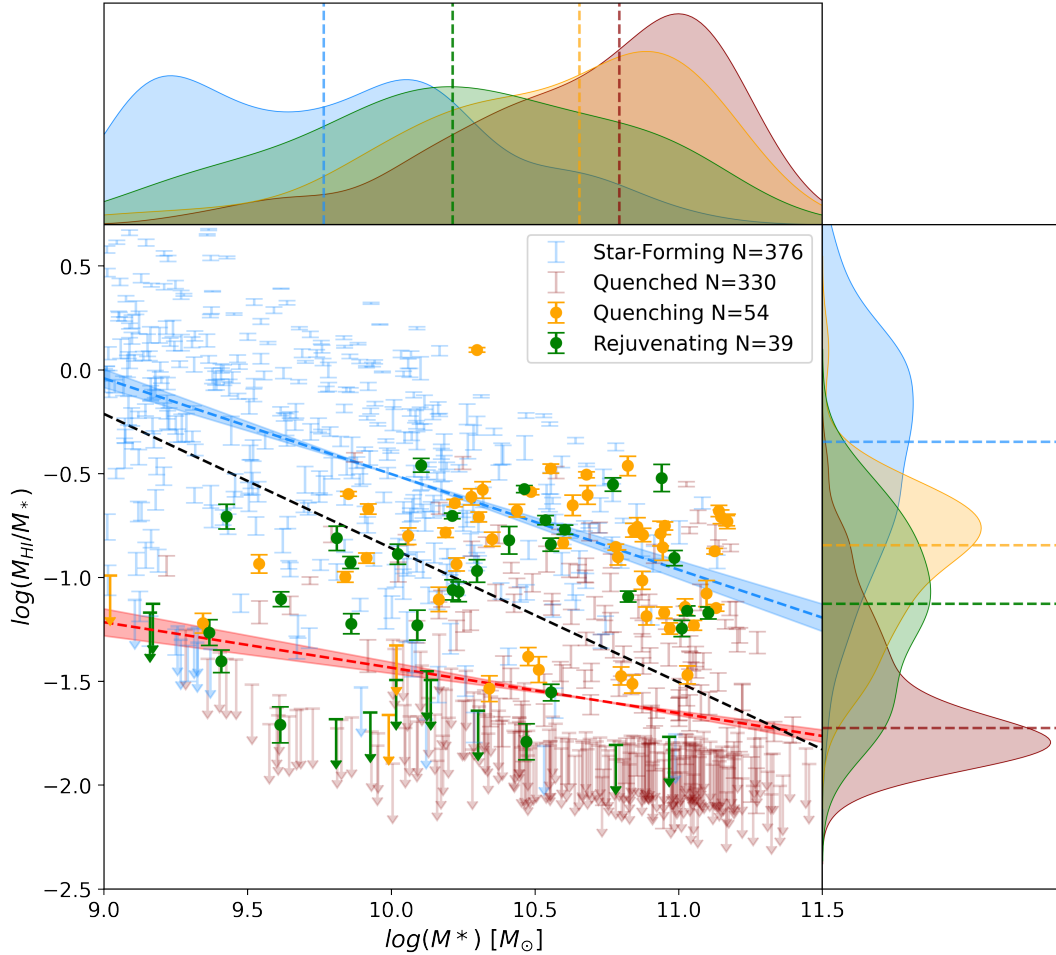


Figure 3.3: HI mass fraction versus stellar mass for the xGASS Representative Sample. Stellar mass and HI mass fraction KDE distributions are shown above and to the right of the main plot. The dashed lines represent the median value of each distribution. Rejuvenating, quenching, star-forming, and quenched galaxies are coloured green, yellow, blue, and red, respectively. Upper limits on the non-detections are represented by downward pointing arrows. Error bars on the data points are obtained from GASS, ALFALFA, and the HI Cornell Archive, representing systematic and statistical uncertainties derived from HI spectra. OLS fits are plotted as coloured dashed lines for the star-forming and quenched populations, with the shaded region representing the error on the fit. The black dashed line shows an OLS fit to the full sample.

population are upper limits. The true distribution of quenched galaxies likely lies below the OLS fit, skewed to lower HI mass fractions than what is shown.

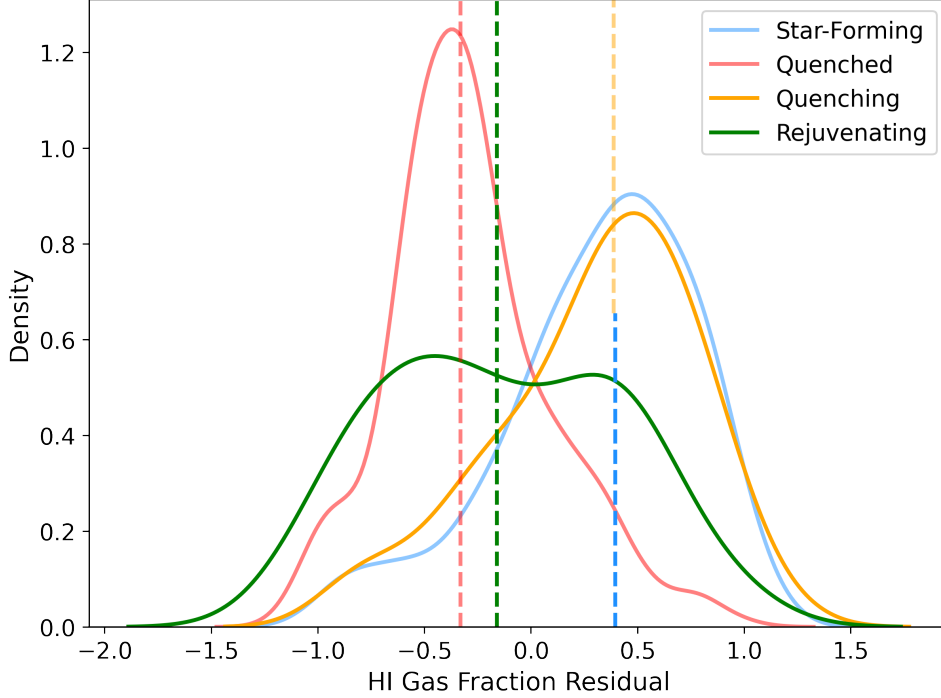


Figure 3.4: HI mass fraction residuals to an OLS fit to the xGASS Representative Sample. Non-detections are included in the distributions using the value of the upper limit. Medians of each distribution are plotted as dashed lines, with overlapping medians in the quenching and star-forming populations. The distributions are smoothed using KDEs.

The rejuvenating and quenching populations occupy similar areas on the plot and thus have similar atomic gas mass fractions for similar masses. However, by comparing these populations to the star-forming and quenched OLS fits, we see that the quenching population is most similar to the star-forming population, while the rejuvenating sample exists between the control populations. A large fraction of the rejuvenating sample are upper limits; therefore the true distribution of the rejuvenating sample is broader than shown, accentuating its

distinction from the star-forming population.

The residuals of the OLS fit to the full xGASS sample are shown in Figure 3.4, where we can see clear differences between the galaxy populations. Notably, quenching galaxies have a similar distribution to star-forming galaxies, with overlapping KDE distributions and medians. Both the quenching and star-forming populations have low fractions of upper limits, with $\sim 6\%$ in the quenching sample and $\sim 3\%$ in the star-forming sample. We ran an Anderson-Darling test on the HI mass fraction residuals of the quenching and star-forming populations, with the p-values given in Table 3.1. We found with high certainty (a p-value of > 0.25) that the two populations are consistent with being drawn from the same distribution. The quenched sample contains over $\sim 60\%$ upper limits, meaning its true distribution is much broader and has a lower median than shown. The rejuvenating sample lies between the quenched and star-forming distributions, with $\sim 25\%$ being upper limits. The EMDs, shown in table 3.1, comparing the rejuvenating to the star-forming and quenched samples without considering upper limits, show that the rejuvenating distribution is more similar to the quenched distribution due to the smaller EMD value comparing rejuvenating to quenched than rejuvenating to star-forming.

| | | EMD | AD p-value |
|--------------|------------------|------|------------|
| Rejuvenating | vs. Star-Forming | 0.45 | 0.001 |
| | vs. Quenched | 0.21 | 0.006 |
| Quenching | vs. Star-Forming | 0.04 | >0.25 |
| | vs. Quenched | 0.58 | 0.001 |

Table 3.1: Statistical test results comparing HI mass fraction residuals.

3.1.3 xCOLD GASS

xCOLD GASS galaxies are randomly drawn from the xGASS Representative Sample. They thus should also be a representative sample of galaxies in their molecular hydrogen abundances. We can, therefore, compare the H_2 mass fractions of the transitional galaxy populations to the star-forming and quenched populations. Figure 3.5 shows the H_2 mass fractions against stellar mass for the four galaxy populations in xCOLD GASS. The four sub-populations show similar stellar mass distributions to xGASS, as expected. We perform fits to the star-forming and quenched populations as for the xGASS sample. The star-forming galaxies align with expectations, with their molecular gas abundances systematically higher than those of the quenched population. The transitional galaxy populations are both seen to be intermediate to the star-forming and quenched samples, with the rejuvenating population more closely sampling the star-forming population.

Similar to Section 3.1.2, Figure 3.6 shows the residuals of the OLS fit to the entire xCOLDGASS sample. The fit to the entire dataset is steeper than those of the individual star-forming or quenched populations because of the overdensities of each sample at low and high stellar masses. The star-forming and rejuvenating samples have similar distributions and similar fractions of non-detections ($\sim 6\%$). This is illustrated by the AD test, where the rejuvenating sample is likely drawn from the same distribution as the star-forming population. The EMD also shows that the rejuvenating sample is most similar to the star-forming control population. We note that the true distributions of the quenched and quenching samples are more gas-poor than what is shown due to

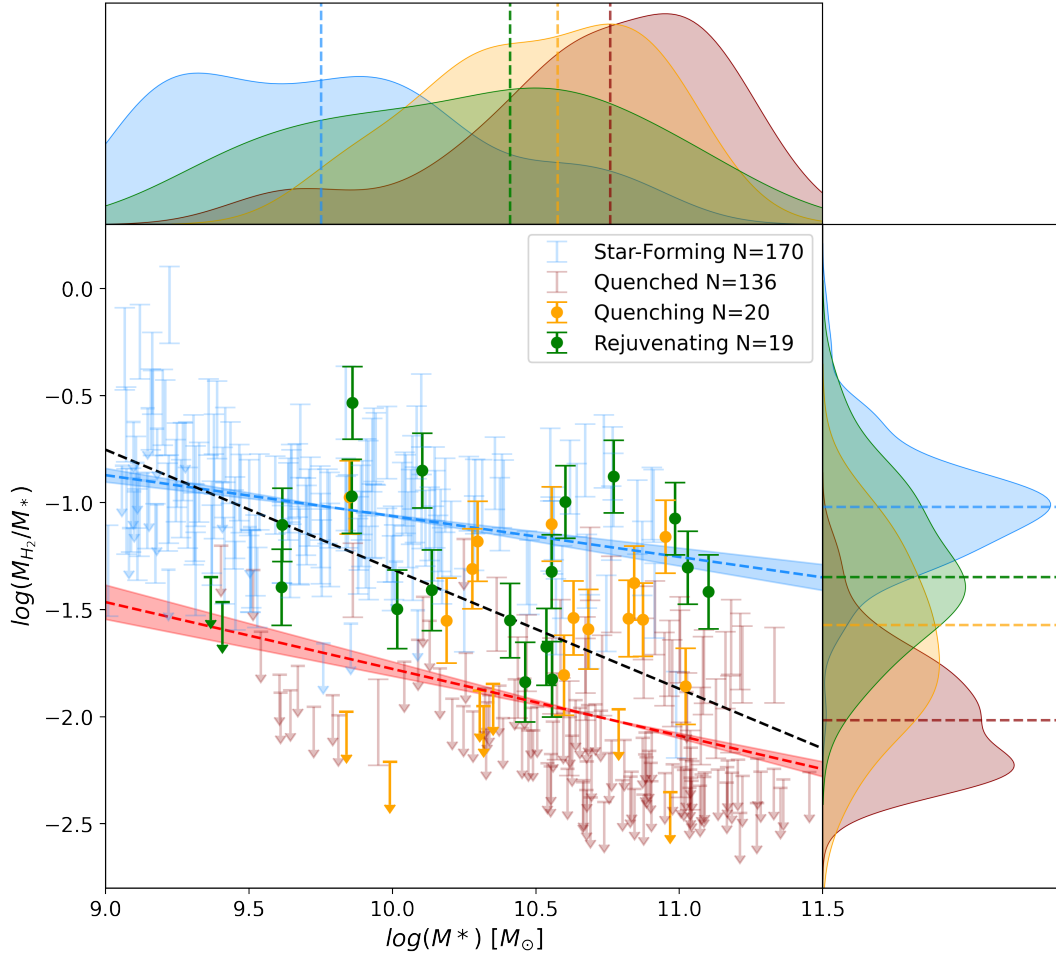


Figure 3.5: H_2 mass fraction versus stellar mass for the xCOLD GASS sample. Stellar mass and H_2 mass fraction KDE distributions are shown above and to the right of the main plot. The dashed lines represent the median value of each distribution. Rejuvenating, quenching, star-forming, and quenched galaxies are coloured green, yellow, blue, and red, respectively. Upper limits on the non-detections are represented by downward pointing arrows. Error bars on the data points are given by uncertainties on the CO(1-0) line measurement and the uncertainty on the CO-to- H_2 conversion factor of 35% from the methodology presented in Accurso et al. (2017). OLS fits are plotted as coloured dashed lines for the star-forming and quenched populations, with the shaded region representing the error on the fit. The black dashed line shows an OLS fit to the full sample.

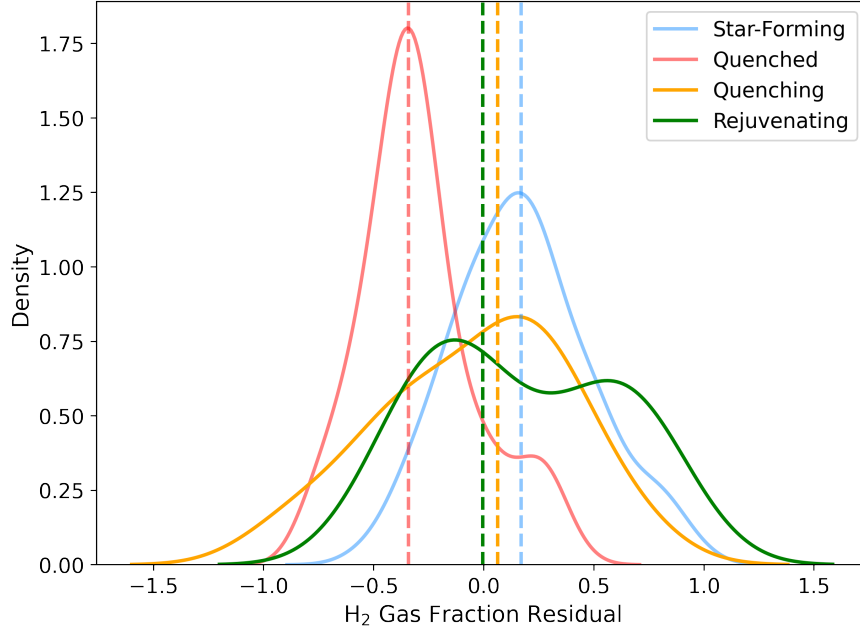


Figure 3.6: The H_2 mass fraction residuals to an OLS fit to the whole xCOLD GASS sample are plotted as KDEs for each galaxy sub-population. The median to each distribution is plotted as dashed lines.

the large fractions of non-detections in the quenched sample ($\sim 74\%$) and the quenching sample ($\sim 35\%$). Because the true distribution of quenched galaxies is more gas-poor, it is less similar to the star-forming distribution than what is shown. This aligns with the expectation that actively quenching galaxies have a depleted gas supply compared to star-forming galaxies.

| | | EMD | AD p-value |
|--------------|------------------|------|------------|
| Rejuvenating | vs. Star-Forming | 0.14 | 0.150 |
| | vs. Quenched | 0.47 | 0.001 |
| Quenching | vs. Star-Forming | 0.21 | 0.013 |
| | vs. Quenched | 0.28 | 0.001 |

Table 3.2: Statistical test results comparing H_2 mass fraction residuals.

3.1.4 Total Gas

With both atomic and molecular gas measurements for each of our galaxy samples, we can derive their total gas ($\text{HI} + \text{H}_2$) fractions. The figures showing the total gas mass fractions of the four populations are shown on the following pages. The features in Figure 3.7 are the same as those presented for the HI and H_2 mass fractions. The upper limits are for galaxies with one or both of the HI and H_2 measurements being non-detections. The star-forming and quenched populations are distinct populations, with star-forming galaxies occupying the high gas mass fraction and low stellar mass regime and the quenched galaxies the low gas mass fraction and high stellar mass regime. The high stellar masses of the quenching sample draw the overall gas mass fraction distribution down, but they seem to trace the star-forming population. There is a similar effect on the rejuvenating population; however, both transitional galaxy populations are, on average, intermediate to the fits of the star-forming and quenched samples.

The residuals to the OLS fit to the xCOLD GASS/xGASS matched sample are shown in Figure 3.8, similar to the plots in the previous sections. Star-forming and quenched galaxies are above and below the line of best fit, respectively. Figure 3.8 shows that the quenching population is similar to the star-forming sample, as confirmed by the Anderson-Darling test. Rejuvenating galaxies present as a distinct intermediate population, with inconclusive Anderson-Darling tests and similar EMDs compared to the star-forming and quenched populations.

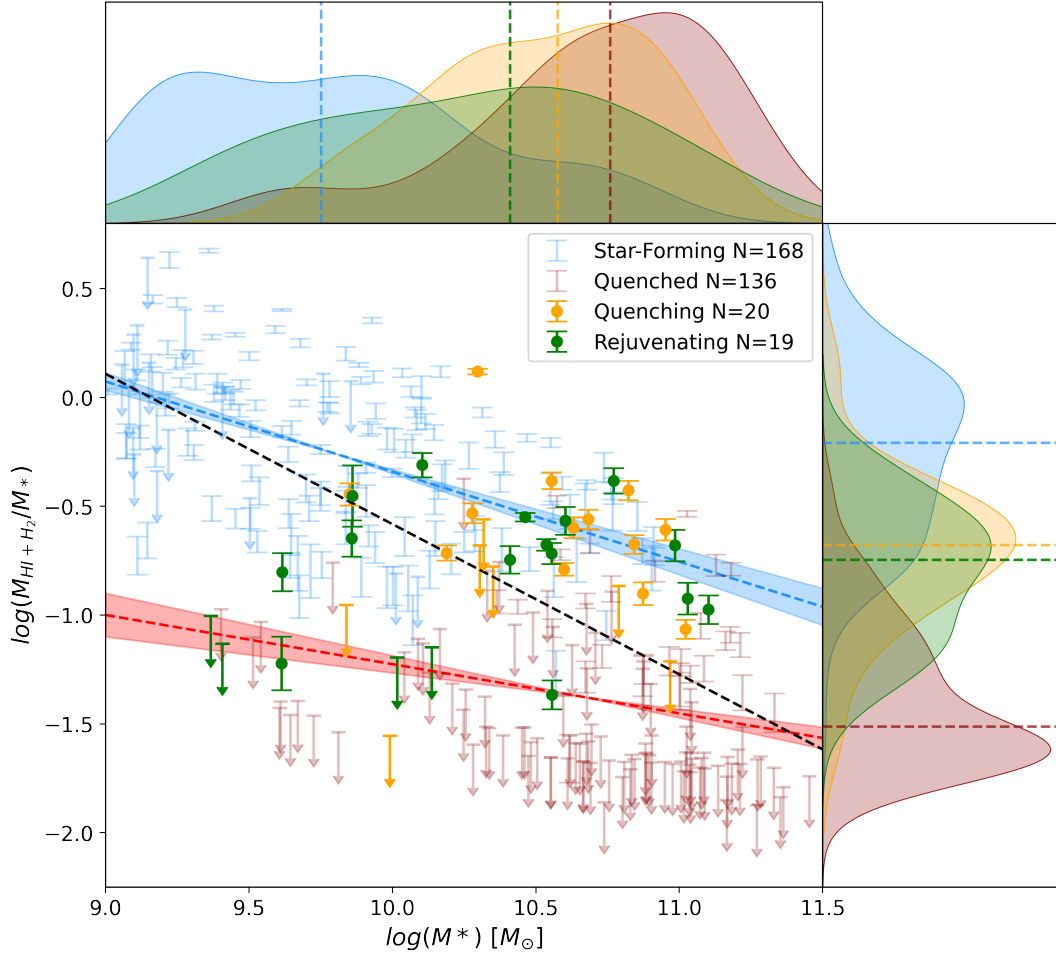


Figure 3.7: Total gas mass fraction versus stellar mass for the xGASS/xCOLD GASS matched sample. Stellar mass and total gas mass fraction KDE distributions are shown above and to the right of the main plot. The dashed lines represent the median value of each distribution. Rejuvenating, quenching, star-forming, and quenched galaxies are coloured green, yellow, blue, and red, respectively. Upper limits on the non-detections are represented by downward pointing arrows. Error bars are calculated through propagation from HI and H₂ mass uncertainties. OLS fits are plotted as coloured dashed lines for the star-forming and quenched populations, with the shaded region representing the error on the fit. The black dashed line shows an OLS fit to the full sample.

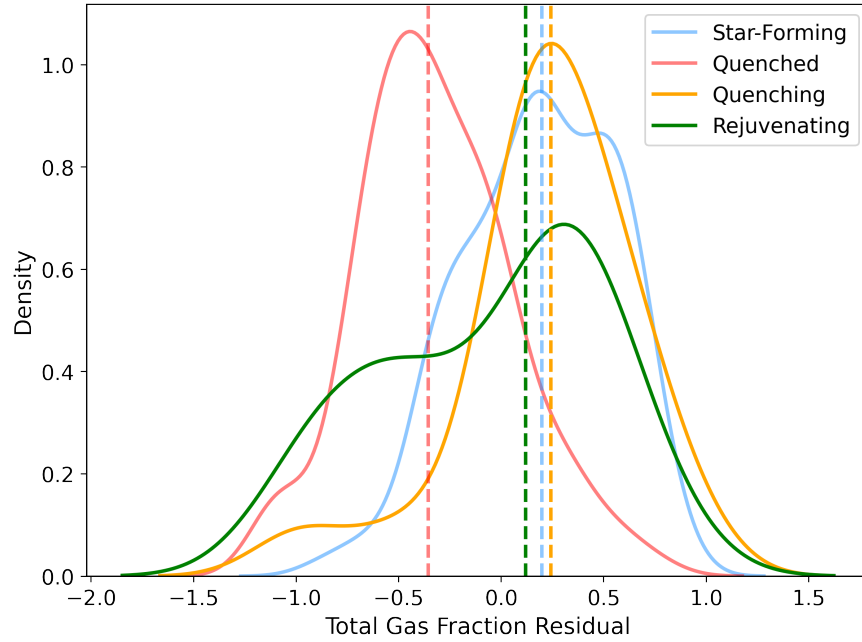


Figure 3.8: Residuals to the OLS fit to the total ($\text{HI} + \text{H}_2$) mass fractions of the full xCOLD GASS/xGASS matched sample. The distributions are smoothed using KDEs. Medians to each distribution are plotted as vertical dashed lines.

| | | EMD | AD p-value |
|--------------|------------------|------|------------|
| Rejuvenating | vs. Star-Forming | 0.24 | 0.015 |
| | vs. Quenched | 0.30 | 0.003 |
| Quenching | vs. Star-Forming | 0.10 | >0.25 |
| | vs. Quenched | 0.54 | 0.001 |

Table 3.3: Statistical test results comparing total gas mass fraction residuals.

3.2 Derived Gas Properties

With reliable atomic and molecular gas data, we can determine various derived gas properties for our four galaxy populations. First, in Section 3.2.1, we show how long it will take for a galaxy to consume its short and long-term star-forming gas reserves using star formation rates from the MPA-JHU SDSS catalogue, computed primarily using emission lines. For an average galaxy, we expect depletion time to increase with stellar mass for both the H_2 and total gas reserves (Saintonge et al., 2017; Díaz-García & Knapen, 2020). In Section 3.2.2, we show the distribution of H_2 to HI gas mass fractions against stellar mass. This measure provides insight into how efficiently a galaxy converts its atomic gas to molecular gas and whether it is accreting pristine gas from the IGM, as discussed in Section 1.1.6. Previous work has shown that early-type and late-type galaxies have differing trends in their H_2 -to-HI ratios with stellar mass, respectively, showing mildly increasing and decreasing relations (Calette et al., 2018).

3.2.1 Depletion Time

Depletion time is sensitive to the timescales associated with the SFR metric used. Our transitional galaxy populations have significantly evolved their SFRs in the past $\sim 100\text{Myr}$; therefore, we cannot use SED or UV-based SFR tracers, as they typically trace longer timescales, discussed in Section 1.1.3. We use the MPA-JHU emission line-derived SFRs using the Brinchmann et al. (2004) method, as these are on a more instantaneous timescale, discussed in Section

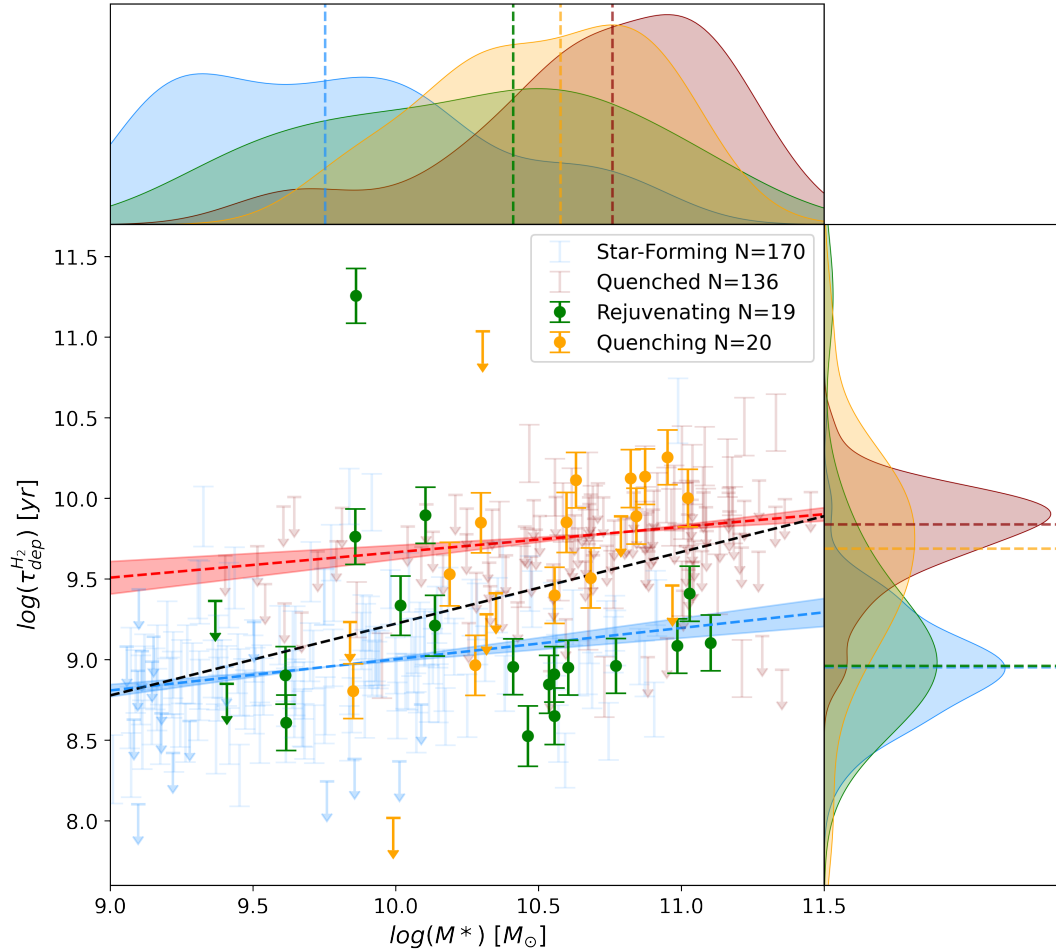


Figure 3.9: H_2 depletion time versus stellar mass for the xGASS/xCOLD GASS matched sample. Stellar mass and H_2 depletion time KDE distributions are shown above and to the right of the main plot. The dashed lines represent the median value of each distribution. Rejuvenating, quenching, star-forming, and quenched galaxies are coloured green, yellow, blue, and red, respectively. Upper limits on the non-detections are represented by downward pointing arrows. Error bars are calculated through propagation from HI and H_2 mass uncertainties. OLS fits are plotted as coloured dashed lines for the star-forming and quenched populations, with the shaded region representing the error on the fit. The black dashed line shows an OLS fit to the full sample.

1.1.3. Emission line-derived SFRs are beneficial, as a long-term average SFR from SED fitting does not account for the changes that the transitional galaxy populations have recently undergone.

Figure 3.9 shows the H_2 depletion times versus stellar masses of the four galaxy populations. We find a slightly increasing trend in the normal star-forming and quenched populations, with quenched galaxies having higher depletion times than star-forming galaxies across all stellar masses. However, the true distribution of quenched galaxies is lower than shown due to the large number of upper limits on the H_2 depletion times for this population. We see that the τ_{dep} of rejuvenating galaxies tend to lie closer to the star-forming population and that the quenching galaxies tend to lie closer to the quenched population. At low stellar masses, several rejuvenating galaxies have depletion times higher than the star-forming average due to their comparatively low SFRs.

Figure 3.10 shows the total gas depletion times for our four galaxy populations. Galaxies plotted with upper limits in Figure 3.10 have an upper limit on either one or both of the HI or H_2 measurements. While the global trend shows increasing total gas depletion time with stellar mass, star-forming galaxies have a slight decrease in depletion time with stellar mass. Similar to the trends in Figure 3.9, the τ_{dep} of rejuvenating galaxies are most similar to the star-forming population, and the quenching galaxies are most similar to the quenched population. We also see that, on average, quenching galaxies have a slightly longer depletion time than the quenched population. As seen in Figure 3.9, the rejuvenating galaxies tend to sample the lower end of the star-forming distribution.

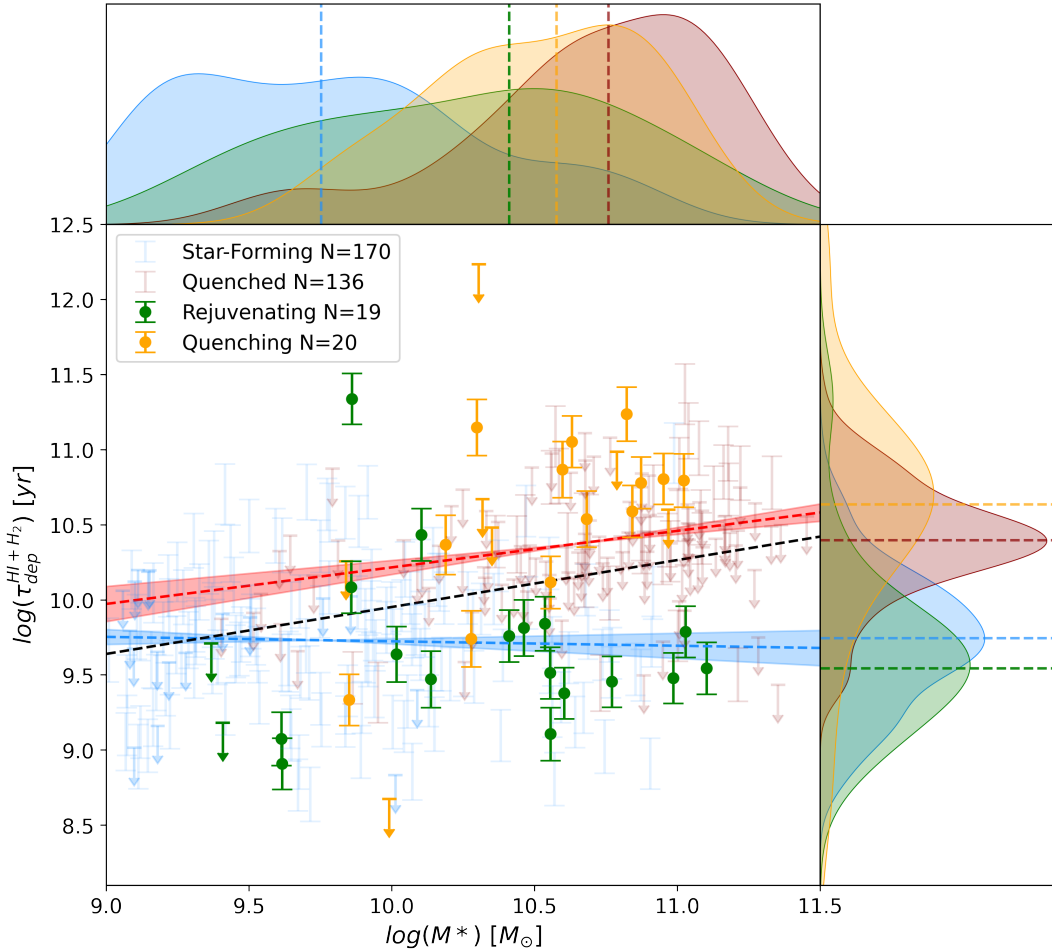


Figure 3.10: Total gas depletion time versus stellar mass for the xGASS/xCOLD GASS matched sample. Stellar mass and total gas depletion time KDE distributions are shown above and to the right of the main plot. The dashed lines represent the median value of each distribution. Rejuvenating, quenching, star-forming, and quenched galaxies are coloured green, yellow, blue, and red, respectively. Upper limits on the non-detections are represented by downward pointing arrows. Error bars are calculated through propagation from HI and H₂ mass uncertainties. OLS fits are plotted as coloured dashed lines for the star-forming and quenched populations, with the shaded region representing the error on the fit. The black dashed line shows an OLS fit to the full sample.

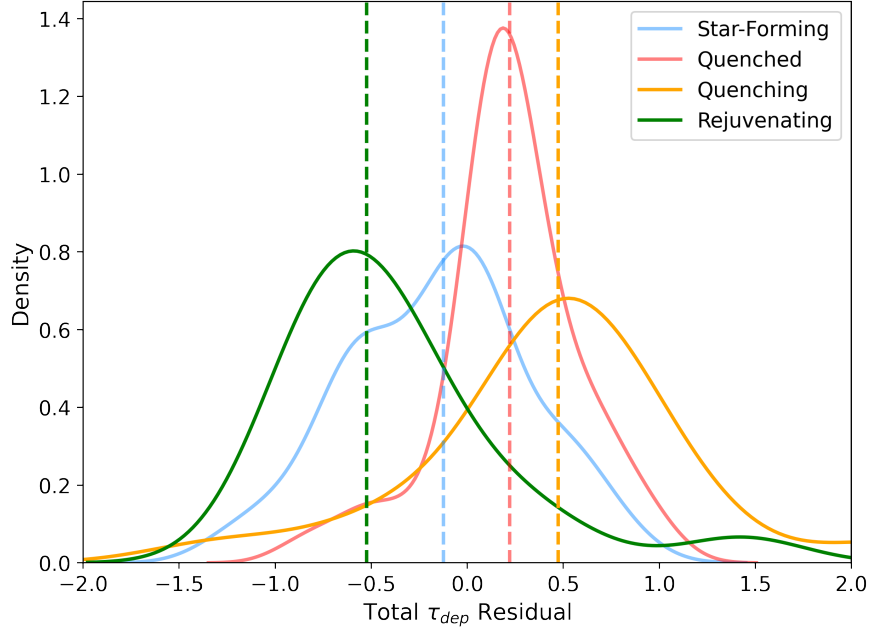


Figure 3.11: Residuals to the OLS fit to the total (HI+H₂) depletion times of the full xCOLD GASS/xGASS matched sample. The distributions are smoothed using KDEs. Medians to each distribution are plotted as vertical dashed lines.

Figure 3.11 shows the residual distributions of the ordinary least squares fit to the full xCOLD GASS/xGASS matched sample. Again, the true quenched distribution is lower than the distribution shown due to the large number of galaxies with upper limits in the sample. The four galaxy populations are distinct, as confirmed using the Anderson-Darling test, with all p-values lower than 0.05 (see Table 3.3). Unlike previous distributions, the rejuvenating and quenching galaxies are not intermediate populations. On average, quenching galaxies have the highest depletion times out of the four populations, while rejuvenating galaxies have the lowest. The short depletion times seen in the rejuvenating population are primarily caused by their low total gas masses.

| | | EMD | AD p-value |
|--------------|------------------|------|------------|
| Rejuvenating | vs. Star-Forming | 0.25 | 0.038 |
| | vs. Quenched | 0.69 | 0.001 |
| Quenching | vs. Star-Forming | 0.70 | 0.001 |
| | vs. Quenched | 0.33 | 0.002 |

Table 3.4: Statistical test results comparing total gas depletion time residuals.

3.2.2 Molecular-to-Atomic Gas Ratio

The molecular-to-atomic gas ratio (H_2/HI) for each galaxy population is shown in Figure 3.12, where we see a significant difference between the rejuvenating and control populations. The OLS fit to the whole xCOLD GASS/xGASS matched sample is shown in black with errors of the fit represented by the shaded region around the line. Non-detections in HI are plotted as lower limits, and non-detections in H_2 as upper limits. We omit galaxies with non-detections in both HI and H_2 . In contrast to what has been found in previous figures, the star-forming and quenched samples follow a similar trend. This trend is likely due to the high fraction of upper limits in both HI and H_2 of the quenched sample. We also see that the quenching population is systematically below the OLS fit and samples the lower end of the quenched population. On the other hand, the rejuvenating sample is systematically above the line of best fit, with 84% of the sample lying above the line. There is a clear trend with lower mass rejuvenating galaxies below $\lesssim 10^{10} M_\odot$, where the average is nearly an order of magnitude above the line of best fit to the total sample.

Figure 3.13 shows the residuals of each population to the OLS fit to the H_2/HI ratio for the full galaxy sample. The rejuvenating sample has an equal

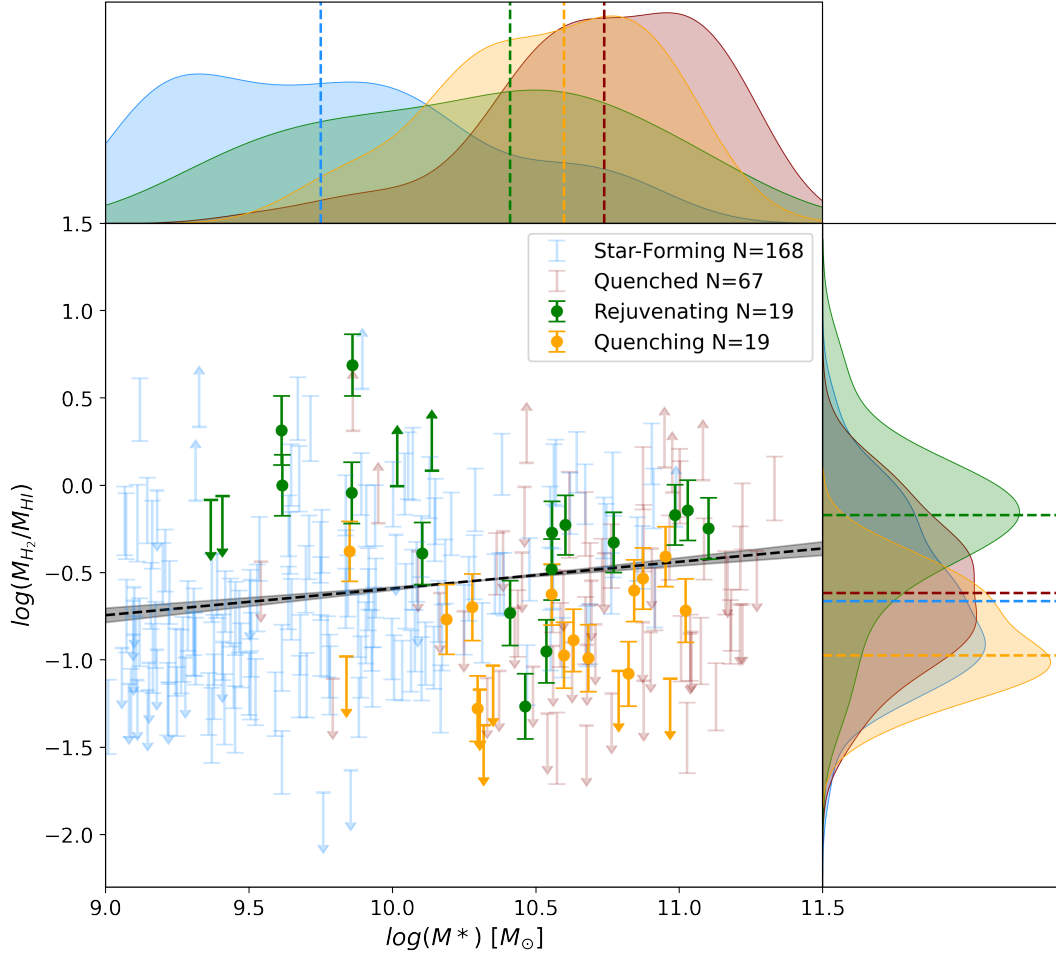


Figure 3.12: Molecular-to-atomic gas ratio versus stellar mass for the xGASS/xCOLD GASS-matched sample. Stellar mass and molecular-to-atomic gas ratio KDE distributions are shown above and to the right of the main plot. The dashed lines represent the median value of each distribution. Rejuvenating, quenching, star-forming, and quenched galaxies are coloured green, yellow, blue, and red, respectively. Upper and lower limits on the non-detections are represented by downward and upward-pointing arrows, respectively. Error bars are calculated through propagation from HI and H₂ mass uncertainties. An OLS fit to the total sample is plotted as a black dashed line, with the shaded region representing the error on the fit.

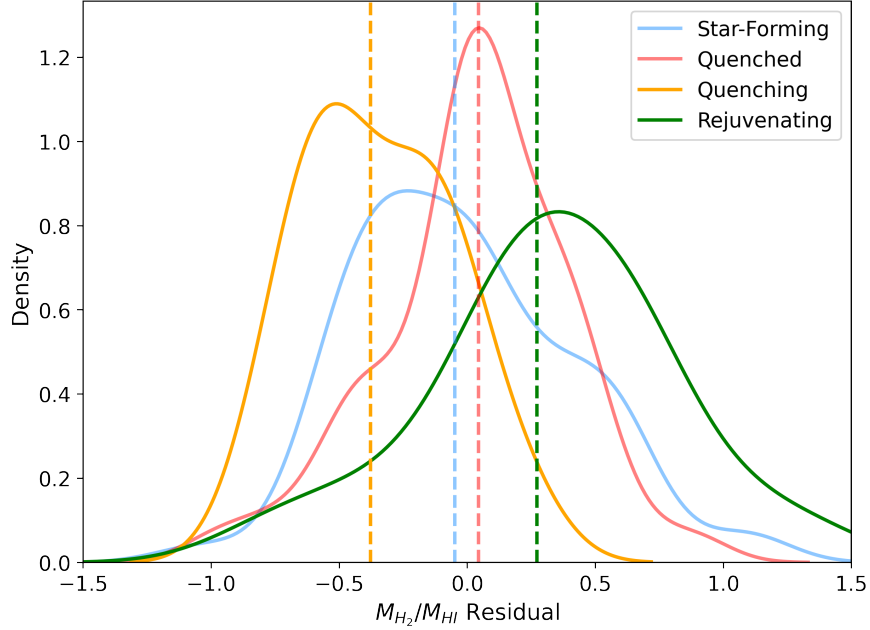


Figure 3.13: Residuals to the OLS fit to the H_2/HI mass ratios of the full xCOLD GASS/xGASS matched sample. Galaxies with non-detections in both HI and H_2 are omitted from the data. The distributions are smoothed using KDEs. Medians to each distribution are plotted as vertical dashed lines.

number of upper and lower limits; therefore, the overall distribution is likely similar to the true measurements. The star-forming sample contains slightly more H_2 than HI non-detections; thus, the true distribution would shift to the left. Most quenched galaxies are omitted as upper limits dominate the H_2 and HI measurements. The quenching sample contains 35% H_2 and 5% HI non-detections, so the true median of the distribution is likely significantly lower than what is shown. Therefore, the rejuvenating sample is an even more distinct population than shown, as it is the only population without a higher fraction of H_2 non-detections compared to HI. The Anderson-Darling p-values are all low, as shown in Table 3.5, suggesting that quenching and rejuvenating galaxies are both drawn from different distributions than the control populations.

| | | EMD | AD p-value |
|--------------|------------------|------|------------|
| Rejuvenating | vs. Star-Forming | 0.35 | 0.001 |
| | vs. Quenched | 0.30 | 0.001 |
| Quenching | vs. Star-Forming | 0.33 | 0.001 |
| | vs. Quenched | 0.38 | 0.001 |

Table 3.5: Statistical test results for comparing molecular-to-atomic gas ratio residual distributions.

3.3 Gas Phase Metallicity

A high metallicity of the ISM promotes cooling and, in turn, H_2 formation, as discussed in Section 1.1.7. This motivates the exploration of the gas-phase metallicity of the rejuvenating population, as the galaxies have high molecular-to-atomic gas ratios, particularly at the low stellar mass end.

We use two approaches to calculate our metallicities for our galaxy populations, with both metrics using emission lines. As the quenching and quenched populations do not have high signal-to-noise emission line measurements, we do not include them in this section. The star-forming and rejuvenating populations have robust emission line measurements; therefore, we can derive gas-phase metallicities for large fractions of the samples.

3.3.1 Full Sample

We first explore the gas-phase metallicities of the rejuvenating and star-forming samples using the O3N2 metric (Marino et al., 2013). This method uses the ratios of the OIII and NII fluxes to those of hydrogen Balmer lines, $H\alpha$ and $H\beta$.

The following equation gives the O3N2 diagnostic,

$$\text{O3N2} = \log \left(\frac{\text{OIII}/\text{H}\beta}{\text{NII}/\text{H}\alpha} \right). \quad (3.3.1)$$

As shown in Marino et al. (2013) using electron temperature calibrated oxygen abundances, the O3N2 metric provides reliable measurements between values of $-1.1 < \text{O3N2} < 1.7$, therefore we exclude all galaxies which fall outside this range. We also exclude all galaxies with poor signal-to-noise in each emission line (< 3). After making these cuts, we keep 3,948/5,075 rejuvenating galaxies and 104,384/114,565 star-forming galaxies. It is worth noting that a higher proportion of star-forming galaxies are removed from the sample due to the measurements falling above the Marino et al. (2013) range, which indicates a lower gas-phase metallicity.

We use the calibration from Marino et al. (2013) to convert our O3N2 values to oxygen abundance by

$$12 + \log(\text{O}/\text{H}) = 8.533[\pm 0.012] - 0.214[\pm 0.012] \times \text{O3N2}. \quad (3.3.2)$$

Figure 3.14 shows the oxygen abundances given by the O3N2 metric of the rejuvenating population compared to the star-forming population. The percentages indicate the proportion of galaxies that survive the cuts on the data. Galaxies are primarily removed from the star-forming sample due to lying outside the valid range of the O3N2 metric, whereas galaxies are removed from the rejuvenating sample primarily due to failing the signal-to-noise cut. The rejuvenating galaxies have lower numbers of reliable metallicity measurements

at all stellar masses. This indicates that compared to the star-forming sample, rejuvenating galaxies have higher metallicities than plotted as OIII emission is weak compared to the other sources of emission used in equation 3.3.1, and thus we exclude some galaxies with higher metallicities. We find a clear trend of rejuvenating galaxies with higher gas-phase metallicities compared to the star-forming population at stellar masses below $\sim 10^{10} M_{\odot}$.

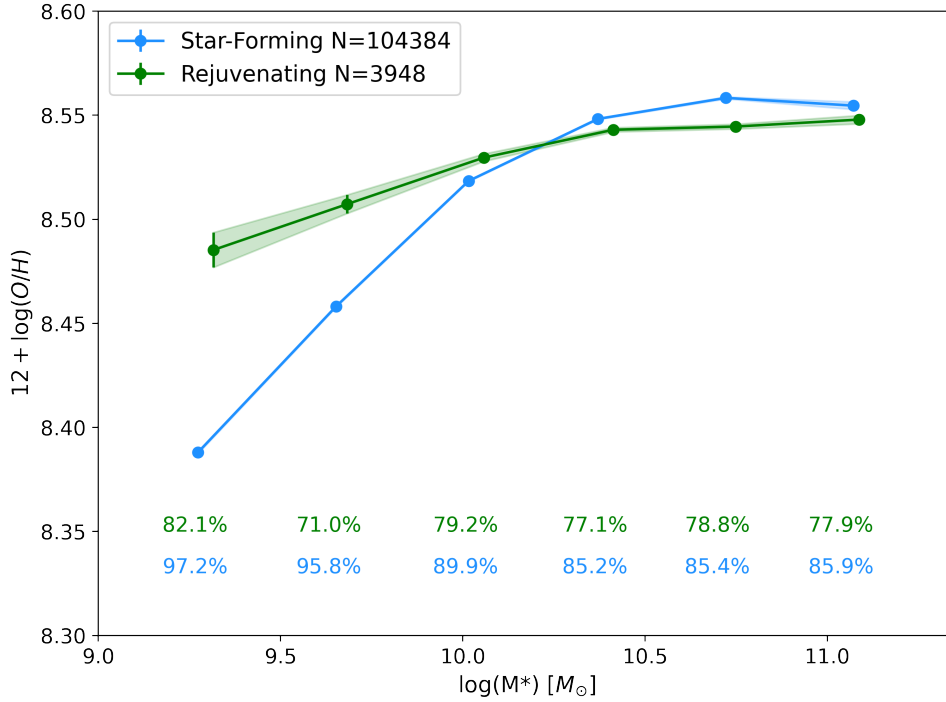


Figure 3.14: O3N2 derived gas-phase metallicity versus stellar mass for the star-forming and rejuvenating populations. Galaxies are binned by stellar mass, with points and error bars showing the mean and standard error on the metallicity and stellar mass of each bin. The percentages indicate the number of galaxies in each stellar mass bin remaining after applying data quality cuts.

While the O3N2 metric allows us to keep large numbers of galaxies in our samples, we turn to MPA-JHU (Kauffmann et al., 2003a) derived gas-phase metallicities, given their improved methodology. These metallicities account

for more emission lines, as well as dust correction, which significantly improves their reliability. The emission lines used in the calculation of the gas-phase metallicities provided in MPA-JHU, following the methodology in Tremonti et al. (2004), are $H\alpha$, $H\beta$, OIII, OII, NII, and SII. As discussed in Section 3.4, the rejuvenating sample is more affected by dust effects, which can cause the average population to deviate from the true distribution. However, using the MPA-JHU oxygen abundances, we exclude more galaxies from analysis due to data quality cuts. These measurements require good data on more emission lines, and several emission lines have stricter signal-to-noise cuts (> 5).

The MPA-JHU-derived gas-phase metallicities are shown in Figure 3.15, where we lose significantly more galaxies due to the stricter data filtering process. The oxygen abundances are higher than with the O3N2 metric because of the dust corrections applied to the emission lines in MPA-JHU. The rejuvenating population exhibits a similar trend to the larger sample from Figure 3.14, with a more pronounced difference in their gas phase metallicities in the low stellar mass region. The fractions of reliable measurements kept as part of the MPA-JHU filtering process are significantly lower for rejuvenating galaxies than star-forming galaxies at the stellar mass end. Considering that galaxies with poor emission line measurements are discarded, the true distribution of rejuvenating galaxies is higher than shown.

Previous studies have shown that gas-phase metallicity depends on stellar mass and global star formation rate (Mannucci et al., 2010; Brown et al., 2018). Lower global SFRs generally correlate with a higher gas-phase metallicity, as

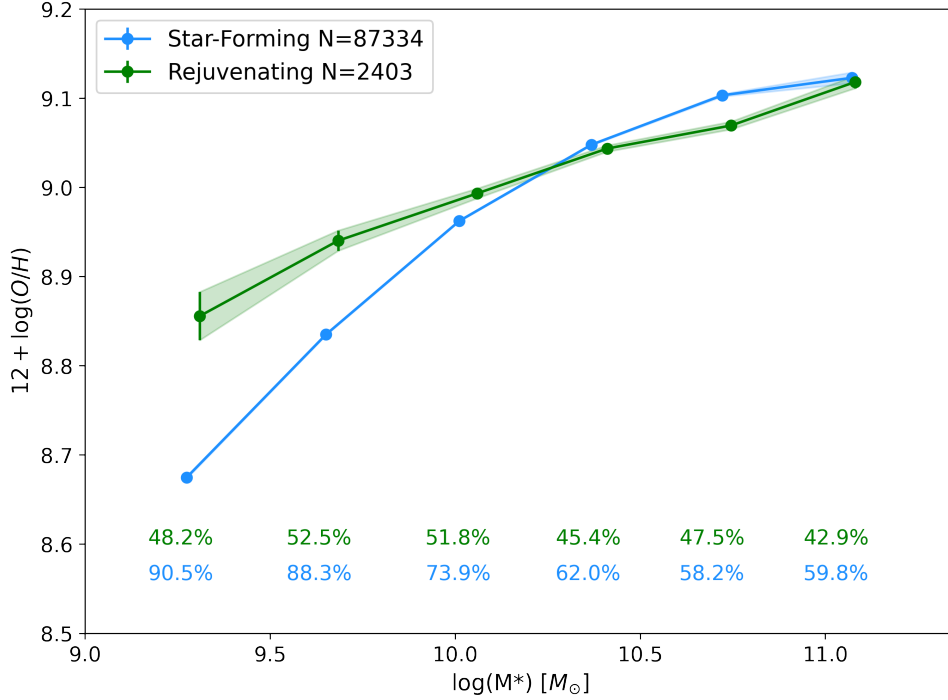


Figure 3.15: MPA-JHU gas-phase metallicity versus stellar mass for the star-forming and rejuvenating populations. Galaxies are binned by stellar mass, with points and error bars showing the mean and standard error on the metallicity and stellar mass of each bin. The percentages indicate the number of galaxies in each stellar mass bin remaining after applying data quality cuts.

discussed in Section 1.1.7, and the rejuvenating population has lower star formation rates than star-forming galaxies on average. Therefore, the differences in gas phase metallicity may be due to differences in SFR. To test this, we create a mass and SFR-matched sample by first binning the star-forming and rejuvenating samples by stellar mass using bins of equal width. Within each stellar mass bin, for each rejuvenating galaxy, we selected the star-forming galaxy with the closest SFR, thereby creating a 1:1 sample. Figure 3.16 shows the SFR-matched star-forming sample compared to the original star-forming and rejuvenating samples. We can see that the rejuvenating sample still lies above

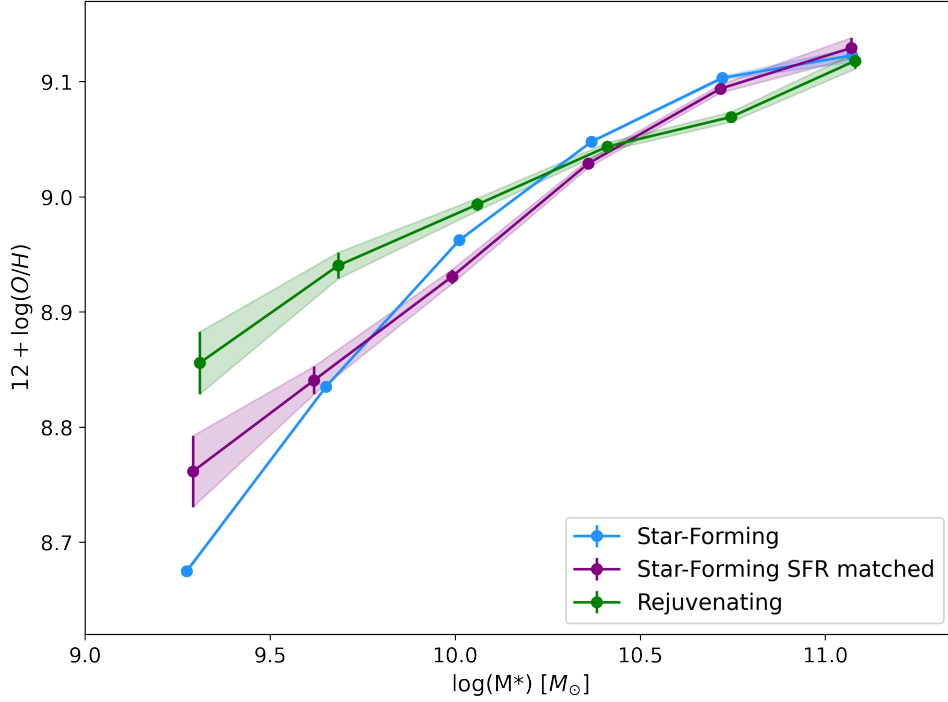


Figure 3.16: MPA-JHU gas-phase metallicity versus stellar mass for the star-forming and rejuvenating populations, with a sub-sample of star-forming galaxies that is SFR matched to the rejuvenating sample. Galaxies are binned by stellar mass, with points and error bars showing the mean and standard error on the metallicity and stellar mass of each bin.

both star-forming samples at the low mass end, though with lower certainty, given the larger error bars on the matched star-forming sample. This shows that our result that the rejuvenating sample has systematically high gas-phase metallicities at low stellar mass is not simply due to differences in SFR, and rejuvenating galaxies have enhanced metallicities.

3.3.2 xCOLD GASS Sample

In the previous section, we showed that for a large sample selected from SDSS, rejuvenating galaxies tend to have higher gas-phase metallicities. Here, we explore the metallicity of the sample of galaxies with gas measurements from xCOLD GASS. In Table 3.6, we list all the gas properties of the rejuvenating sample. In Figure 3.17, we show the oxygen abundances for the rejuvenating and binned star-forming samples. With the strict MPA-JHU cuts on the metallicity, we have 13/19 rejuvenating galaxies with reliable data. The trend of low-stellar mass rejuvenating galaxies with high gas-phase metallicities, while with less certainty, holds true even for this small sample with both HI and H₂ measurements; the average metallicity of the low-stellar mass rejuvenating galaxies, as shown by the black point in Figure 3.17, lies above the star-forming sample.

The results for our full parent rejuvenating and star-forming samples from Section 3.3.1 are for a larger redshift range ($z < 0.1$) than for our gas samples ($0.025 < z < 0.05$). In Figure 3.18, we show the gas-phase metallicities for the parent samples in the same redshift range of the gas data. We have a slightly higher percentage of rejuvenating galaxies with reliable metallicities within this redshift range ($\sim 60\%$ vs. $\sim 47\%$). We see the same trend as in Figures 3.15, 3.16, and 3.17, where low stellar mass rejuvenating galaxies have high gas-phase metallicities compared to normal star-forming galaxies. The difference in gas-phase metallicities between the two samples is smaller than in previous figures.

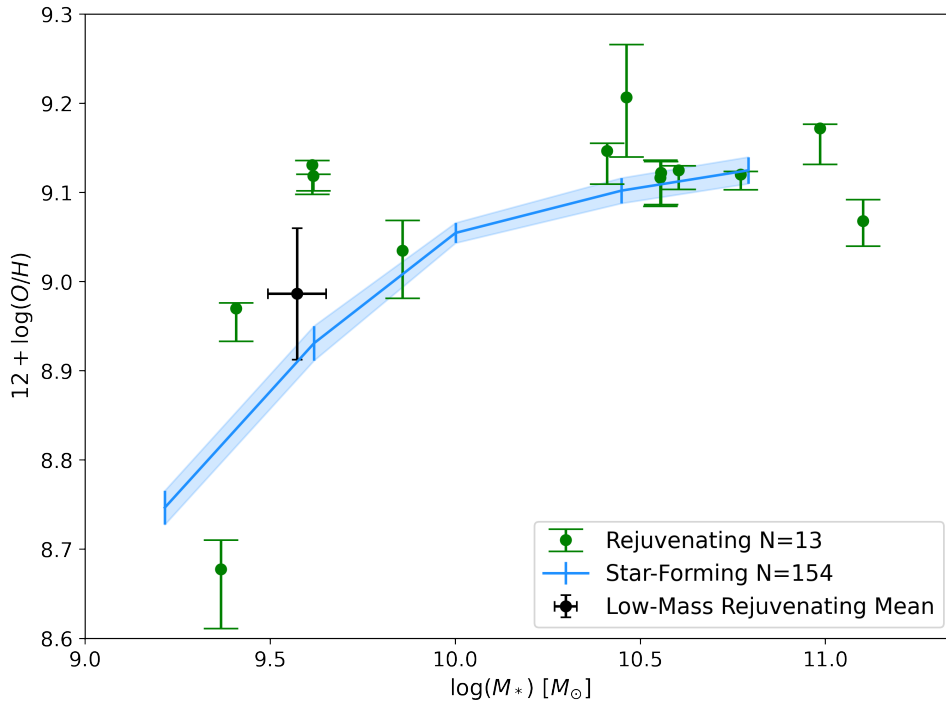


Figure 3.17: MPA-JHU gas-phase metallicity versus stellar mass for the star-forming and rejuvenating populations with gas measurements from xCOLD GASS. Star-forming galaxies are binned by stellar mass, with error bars showing the mean and standard error on the metallicity and stellar mass of each bin. Rejuvenating galaxies are plotted with error bars representing the 16th and 84th percentiles of the data. The black point is the mean in stellar mass and gas-phase metallicity of the five low-stellar mass rejuvenating galaxies, with standard error.

3.4 Dust Effects on the Rejuvenating Sample

In Section 2.1.4, we discussed the potential effects of dust on our rejuvenating sample, discussing that $H\alpha$ equivalent widths are relatively robust to dust, but NUV flux is more susceptible. Here, we show how we perform the NUV dust correction and how these corrections affect our key results.

We use data from the ALLWISE (Cutri et al., 2013) survey, which contains

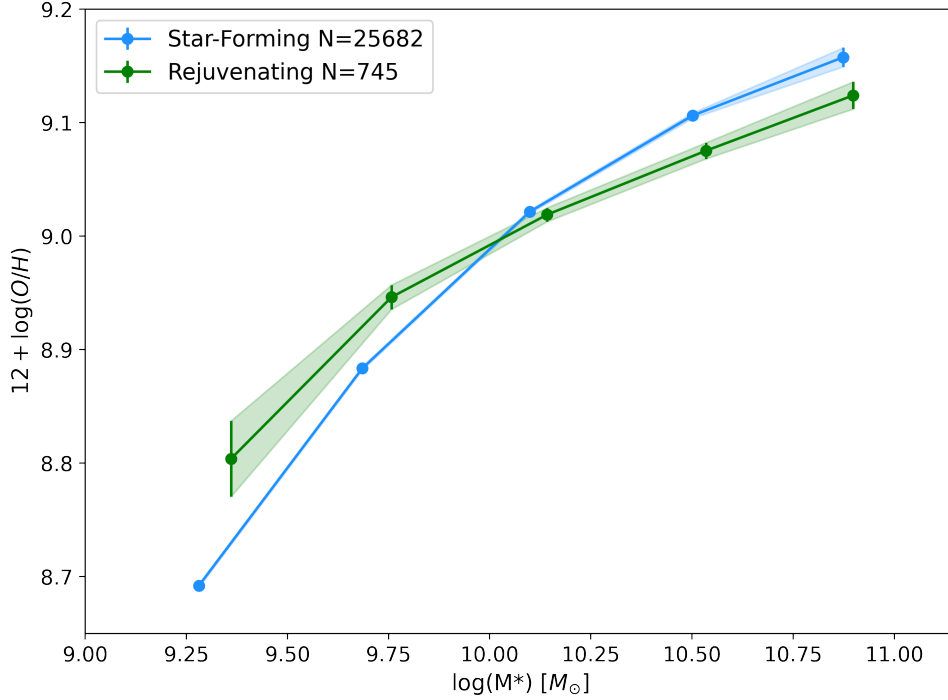


Figure 3.18: MPA-JHU gas-phase metallicity versus stellar mass for the star-forming and rejuvenating populations with redshifts within the xCOLD GASS redshift range of $0.025 < z < 0.05$. Galaxies are binned by stellar mass, with points and error bars showing the mean and standard error on the metallicity and stellar mass of each bin.

magnitudes for four IR bands centred at $3.4\mu\text{m}$ (W1), $4.6\mu\text{m}$ (W2), $12\mu\text{m}$ (W3), and $23\mu\text{m}$ (W4). All galaxies in GSWLC-A have supplementary WISE data, so we use this survey over others, e.g., Herschel (Valiante et al., 2016), which has significantly fewer galaxies in its sample. All WISE bands are tracers of warm dust, with band-3 being sensitive to emission from polycyclic aromatic hydrocarbons (PAHs), which are efficient tracers of dust in the ISM. We use W3 to derive $12\mu\text{m}$ luminosity as a proxy for total infrared (TIR) luminosity, a dust emission tracer. We use the calibration from Cluver et al. (2017), derived

using W3 band data, to convert from $L_{12\mu\text{m}}$ to L_{TIR} ,

$$\log(L_{\text{TIR}}) = 2.21[\pm 0.15] + 0.889[\pm 0.018] \times L_{12\mu\text{m}}. \quad (3.4.1)$$

We then correct the NUV data with the TIR luminosities for the entire GALEX-SDSS matched sample of galaxies within our redshift and stellar mass cuts, utilizing the calibration from Hao et al. (2011),

$$L_{\text{NUV}}^{\text{corr.}} = L_{\text{NUV}} + 0.27[\pm 0.02]L_{\text{TIR}}. \quad (3.4.2)$$

With the corrected NUV luminosities, we compare the attenuation factors for the rejuvenating population to the other three populations in Figure 3.19 by comparing the uncorrected to the corrected NUV luminosity. The attenuation factors A_{NUV} plotted are defined as $A_{\text{NUV}} = L_{\text{NUV}}^{\text{corr.}}/L_{\text{NUV}}$. A median A_{NUV} of ~ 3.5 with a standard deviation of ~ 1.9 was found in Burgarella et al. (2005), and the attenuation factors for our populations are in line with expectations. It is clear that the method we use to select rejuvenating galaxies has dust attenuation effects, with the median NUV attenuation for the rejuvenating sample being over twice as high as that for the star-forming population. The quenching and quenched populations do not have reliable attenuation factor data, as dust emission in these galaxies is likely dominated by heating from old stellar populations (Nersesian et al., 2019). We, therefore, choose only to correct the rejuvenating sample for dust effects.

We then redefine our rejuvenating population with a new cut to the corrected sSFR_{NUV} and are left with a parent sample of 1,297 rejuvenating galaxies, as

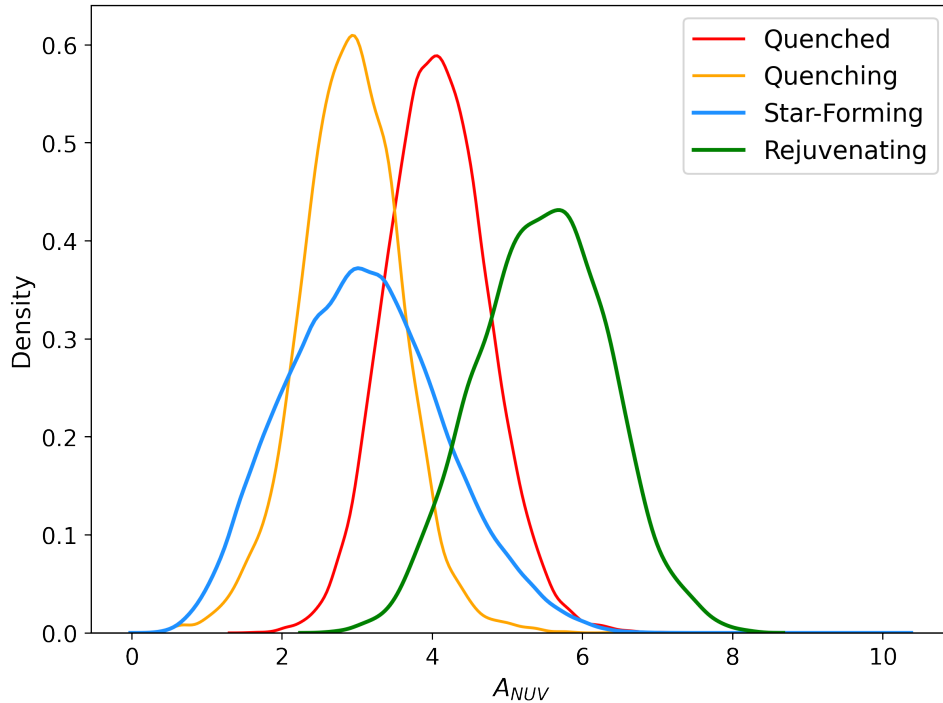


Figure 3.19: Attenuation factor KDE distributions for each parent galaxy population, as calculated using WISE band-3 calibrations (Cluver et al., 2017; Hao et al., 2011).

compared to 5,075 previously. Serendipitously, we are left with nearly half the galaxies in the original gas sample (8/19). On the following pages, I show the updated gas plots with the dust-corrected rejuvenating sample.

Figure 3.20 shows the total gas mass fraction of the dust-corrected rejuvenating sample, with all of the other galaxy populations remaining unchanged. It is worth noting that the stellar mass distributions for the uncorrected and corrected rejuvenating populations are similar, as are the medians for the total gas mass fractions. We still see that the rejuvenating population is intermediate to star-forming and quenched. Figure 3.21 plots the total gas depletion time versus stellar mass with the updated rejuvenating sample. The median of the

new sample is slightly higher than the previous sample, more in line with the star-forming population. Though the rejuvenating population has stellar masses more comparable to the quenched population, they still follow depletion times in line with typical star-forming galaxies. The molecular-to-atomic hydrogen ratios of the new rejuvenating sample are shown in Figure 3.22. Although more than half the sample of rejuvenating galaxies is lost post-dust-correction, the trend of relatively high abundances of H_2 is still seen, especially at low stellar mass. The median of the rejuvenating distribution is approximately three times higher than that of the star-forming population.

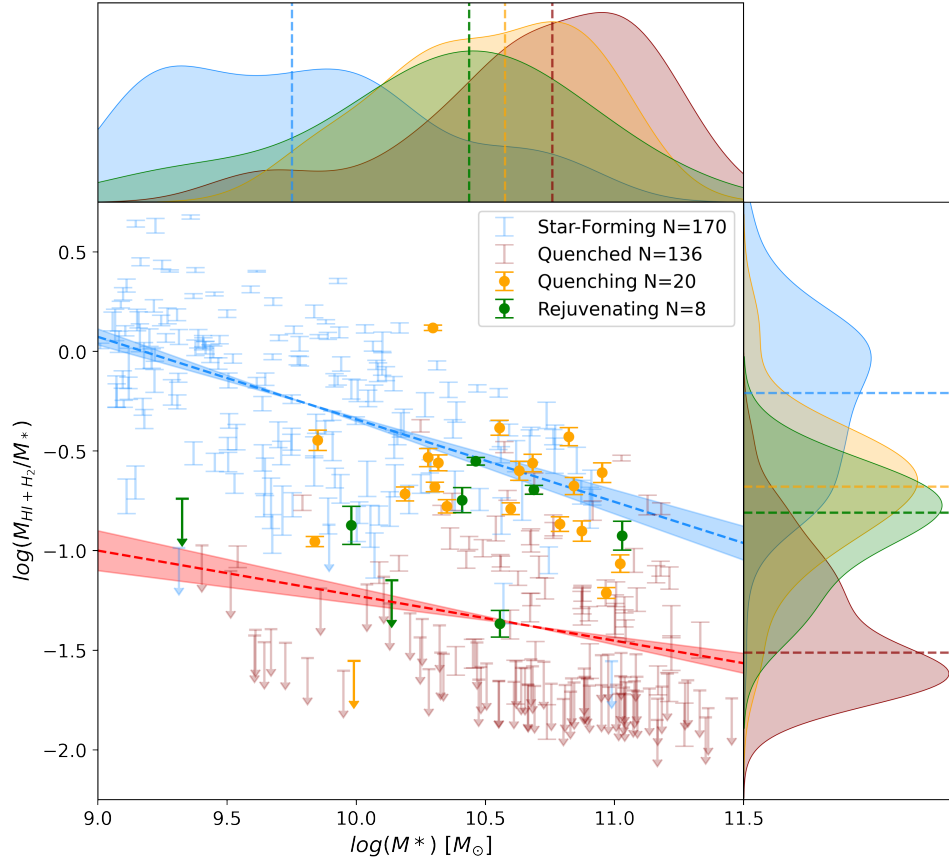


Figure 3.20: Dust corrected total gas mass fraction versus stellar mass for the xGASS/xCOLD GASS matched sample, as in the uncorrected Figure 3.7. Stellar mass and total gas mass fraction KDE distributions are shown above and to the right of the main plot. The dashed lines represent the median value of each distribution. Rejuvenating, quenching, star-forming, and quenched galaxies are coloured green, yellow, blue, and red, respectively. Upper limits on the non-detections are represented by downward pointing arrows. Error bars are calculated through propagation from HI and H₂ mass uncertainties. OLS fits are plotted as coloured dashed lines for the star-forming and quenched populations, with the shaded region representing the error on the fit. The black dashed line shows an OLS fit to the full sample.

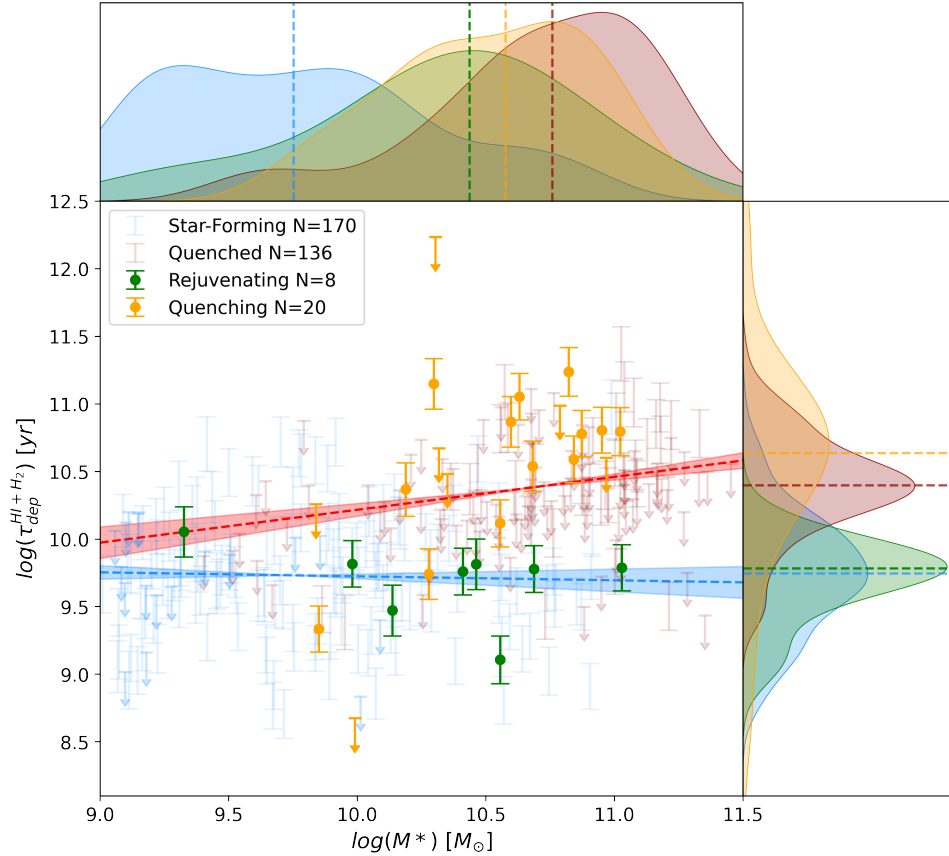


Figure 3.21: Dust corrected total gas depletion time versus stellar mass for the xGASS/xCOLD GASS matched sample, as in the uncorrected Figure 3.10. Stellar mass and total gas depletion time KDE distributions are shown above and to the right of the main plot. The dashed lines represent the median value of each distribution. Rejuvenating, quenching, star-forming, and quenched galaxies are coloured green, yellow, blue, and red, respectively. Upper limits on the non-detections are represented by downward pointing arrows. Error bars are calculated through propagation from HI and H₂ mass uncertainties. OLS fits are plotted as coloured dashed lines for the star-forming and quenched populations, with the shaded region representing the error on the fit.

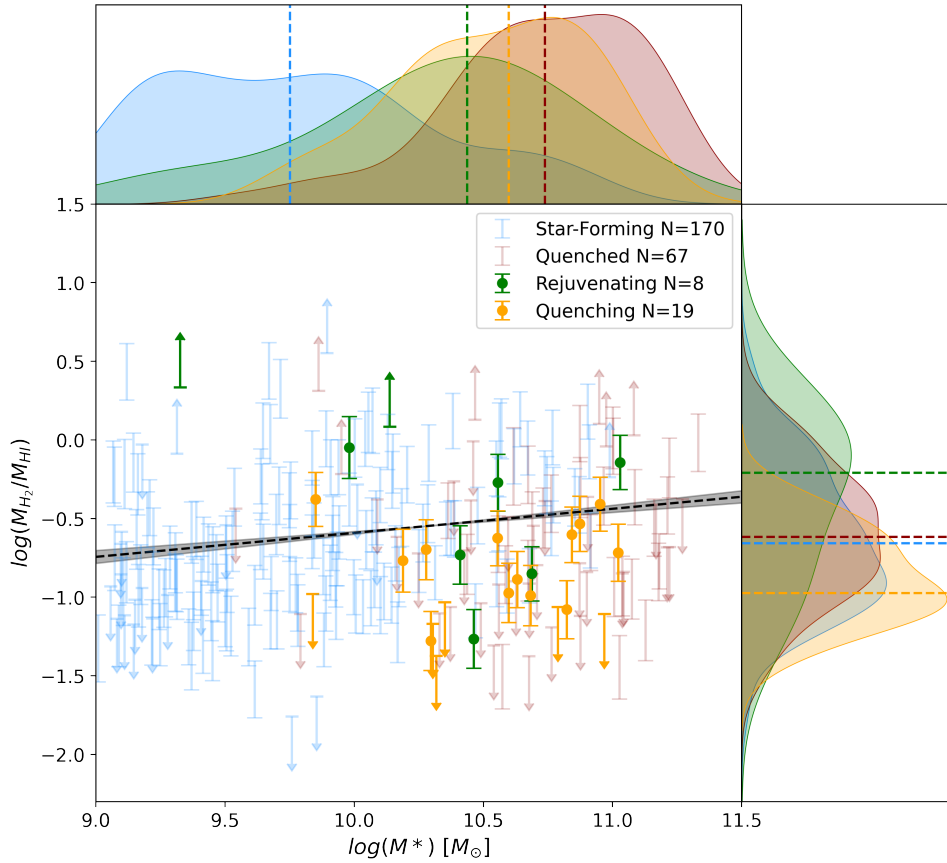


Figure 3.22: Dust corrected molecular-to-atomic gas ratio versus stellar mass for the xGASS/xCOLD GASS-matched sample, as in the uncorrected Figure 3.12. Stellar mass and molecular-to-atomic gas ratio KDE distributions are shown above and to the right of the main plot. The dashed lines represent the median value of each distribution. Rejuvenating, quenching, star-forming, and quenched galaxies are coloured green, yellow, blue, and red, respectively. Upper and lower limits on the non-detections are represented by downward and upward-pointing arrows, respectively. Error bars are calculated through propagation from HI and H₂ mass uncertainties. An OLS fit to the total sample is plotted as a black dashed line, with the shaded region representing the error on the fit.

| RA | DEC | z | M_* | SFR | $\frac{M_{HI}}{M_*}$ | $\frac{M_{H_2}}{M_*}$ | $\frac{M_{HI}+M_{H_2}}{M_*}$ | τ_{dep} | τ_{dep}^{tot} | $\frac{H_2}{HI}$ | $12+\log(O/H)$ |
|------------|-----------|-------|-------------|----------------|----------------------|-----------------------|------------------------------|--------------|--------------------|------------------|----------------|
| deg. | deg. | | $[M_\odot]$ | $[M_\odot/yr]$ | [dex] | [dex] | [dex] | [dex, yr] | [dex, yr] | | |
| 122.550740 | 22.772291 | 0.016 | 9.37 | 0.05 | -1.26 | -1.35* | -1.00* | 9.37* | 9.71* | -0.08* | 8.68 |
| 27.221373 | 13.423945 | 0.016 | 9.41 | 0.12 | -1.40 | -1.46* | -1.13* | 8.85* | 9.18* | -0.06* | 8.97 |
| 179.605960 | 25.09765 | 0.014 | 9.61 | 0.21 | -1.71 | -1.39 | -1.22 | 8.90 | 9.08 | 0.31 | 9.13 |
| 146.080950 | 9.984789 | 0.010 | 9.62 | 0.80 | -1.10 | -1.10 | -0.80 | 8.61 | 8.91 | 0.00 | 9.12 |
| 198.396990 | 29.12653 | 0.020 | 9.86 | 0.13 | -0.93 | -0.97 | -0.65 | 9.76 | 10.09 | -0.04 | 9.03 |
| 217.149030 | 25.708881 | 0.014 | 9.86 | 0.01 | -1.22 | -0.53 | -0.45 | 11.26 | 11.34 | 0.69 | - |
| 334.153720 | 13.254009 | 0.026 | 10.02 | 0.15 | -1.49* | -1.50 | -1.19* | 9.34 | 9.64* | 0.00** | - |
| 348.376650 | 14.063915 | 0.039 | 10.10 | 0.23 | -0.46 | -0.85 | -0.31 | 9.90 | 10.43 | -0.39 | - |
| 120.844850 | 9.962727 | 0.035 | 10.14 | 0.33 | -1.49* | -1.41 | -1.15* | 9.21 | 9.47* | 0.08** | - |
| 32.903934 | 14.512568 | 0.026 | 10.41 | 0.80 | -0.82 | -1.55 | -0.75 | 8.96 | 9.76 | -0.73 | 9.15 |
| 330.844150 | 12.649342 | 0.027 | 10.46 | 1.25 | -0.57 | -1.84 | -0.55 | 8.53 | 9.81 | -1.26 | 9.21 |
| 140.622000 | 14.462046 | 0.032 | 10.54 | 1.04 | -0.72 | -1.67 | -0.68 | 8.85 | 9.84 | -0.95 | - |
| 33.080757 | 13.612689 | 0.041 | 10.55 | 2.10 | -0.84 | -1.32 | -0.72 | 8.91 | 9.51 | -0.48 | 9.12 |
| 344.361240 | 13.001654 | 0.026 | 10.56 | 1.21 | -1.55 | -1.82 | -1.37 | 8.65 | 9.11 | -0.27 | 9.12 |
| 359.185330 | 13.909856 | 0.036 | 10.60 | 4.53 | -0.77 | -1.00 | -0.57 | 8.95 | 9.38 | -0.23 | 9.12 |
| 229.018630 | 6.847628 | 0.037 | 10.77 | 8.54 | -0.55 | -0.88 | -0.38 | 8.96 | 9.46 | -0.33 | 9.12 |
| 154.159970 | 12.577378 | 0.032 | 10.99 | 6.69 | -0.91 | -1.07 | -0.68 | 9.09 | 9.48 | -0.17 | 9.17 |
| 192.871120 | 13.781819 | 0.038 | 11.03 | 2.07 | -1.16 | -1.30 | -0.92 | 9.41 | 9.79 | -0.14 | - |
| 199.892940 | 10.454867 | 0.048 | 11.10 | 3.81 | -1.17 | -1.42 | -0.97 | 9.10 | 9.55 | -0.25 | 9.07 |

Table 3.6: Summary of the gas properties of the rejuvenating sample. Upper and lower limits are shown as * and **, respectively. Stellar masses from GSWLC, line emission-derived SFRs and median gas-phase metallicities from MPA-JHU, HI masses from xGASS Representative Sample, H₂ masses from xCOLD GASS.

Chapter 4

Discussion & Future Work

Using the C&M selection for quenching and rejuvenating galaxies, we deal with short timescale processes on the order of 10^8 years. It was found in C&M that their quenching galaxy sample shows clear dependencies on environment, with higher fractions of quenching galaxies closer to galaxy cluster centres and in higher cluster mass environments. This indicates that quenching more likely occurs in high-density environments. Conversely, the weak environmental dependence of the C&M rejuvenating sample does not help constrain the possible mechanisms driving rejuvenation in the local universe. All of the mechanisms mentioned in Section 1.2.2 could align with the short timescale of the selection method. I will discuss in the following how our results point us in the direction of the possible driving mechanisms of rejuvenating galaxies using the C&M selection method. I then discuss the robustness of our results when corrected for dust effects on the rejuvenating galaxy sample.

1. Both transitional galaxy populations have gas fractions intermediate to the normal star-forming and quenched populations (Figures 3.3, 3.5, and 3.7).

Using a sample of quiescent and early-type galaxies in the ATLAS^{3D} survey (Cappellari et al., 2011) and Herschel Reference Survey (Boselli et al., 2014), Gobat et al. (2020) show that quenched galaxies begin their evolution with a non-negligible amount of gas, and consume their remaining gas over 1.5-2.5 Gyr. Gobat et al. (2020) also show that gas fractions decrease with redshift

as gas is converted into stars, which shows that the average gas fractions of galaxies decrease with time, and that star formation depletes a galaxy’s gas reserve. Our quenching galaxy sample consists of galaxies that have quenched recently, meaning that we are observing the high gas mass end of the quenched population. Since quenching galaxies have just ceased star formation, we expect these galaxies to have consumed their star-forming gas, particularly their short-term gas supply of H_2 .

By definition, rejuvenating galaxies require an inflow of H_2 gas or renewed star formation from instabilities in their existing molecular gas; both of these mechanisms would cause the observed higher gas fractions than the quenched galaxy population, as they rapidly increase the amount of available star-forming gas. Our result agrees with the expectation of the rejuvenating population having high total gas mass fractions compared to the quenched population, as the galaxies need enough gas to produce high star formation rates.

2. The rejuvenating population has depletion times similar to star-forming galaxies, and the quenching population has depletion times similar to quenched galaxies (Figures 3.9 and 3.10).

Quenched and star-forming galaxies are observed to have similar slopes in plots of both H_2 mass and total gas mass versus SFR (Dou et al., 2021; Guo et al., 2021). However, the populations do not occupy the same space in these relations and are shifted in comparison with one another, with star-forming galaxies occupying the low depletion time region, and quenched galaxies occupying the higher depletion time region. This is consistent with our result of

star-forming galaxies having lower depletion times than fully quenched galaxies. In Figures 3.9 and 3.10, which show depletion time as a function of stellar mass, we are likely observing star-forming and quenched galaxies as two distinct populations as the depletion time primarily depends on sSFR, not stellar mass (Huang & Kauffmann, 2014). If we plotted depletion time against sSFR, it is likely that the distinctions between populations would no longer be apparent.

We also find that, on average, quenching galaxies have higher gas fractions than the quenched population. As both populations are classified as “non-star-forming”, but quenching galaxies have more gas as they are recently quenched (Gobat et al., 2020), we expect quenching galaxies to have higher depletion times as they still have a limited supply of gas to consume. However, it is worth noting that the quenching population has uncertain SDSS star formation rates, as they are derived using likelihood distributions as a function of D4000, a proxy for stellar population age, in galaxies where emission lines cannot be used directly, as described in Brinchmann et al. (2004). Additionally, low SFRs in SDSS are systematically over-estimated due to the aperture correction procedure described in Brinchmann et al. (2004). So, we are uncertain if we are probing the true timescale of star formation in quenching galaxies.

We also see that rejuvenating galaxies likely sample from the star-forming population in both H_2 and total gas depletion time versus stellar mass space. While rejuvenating galaxies have different evolutionary histories compared to normal star-forming galaxies, the Kennicutt-Schmidt star formation law holds true. This points towards a general Kennicutt-Schmidt law for galaxies on the SFMS, independent of their star formation histories. Finally, we do not find

that gas-phase metallicity, discussed in point 4, has an impact on the depletion times of rejuvenating galaxies. This is in contrast to the expectation that a higher gas-phase metallicity can correlate with more efficient star formation, as mentioned in Section 1.1.7.

3. Rejuvenating galaxies have high molecular-to-atomic gas ratios at low stellar mass, and quenching galaxies have characteristically low molecular-to-atomic gas ratios (Figure 3.12).

We see a clear difference between the molecular-to-atomic mass ratios of transitional galaxies and control populations. We find that quenching galaxies have low molecular-to-atomic ratios, showing that they have exhausted their molecular hydrogen gas reserves, and something is preventing the conversion of HI to H₂. As these galaxies are preferentially found in dense environments, there are several possible mechanisms that could be causing them to quench, such as major mergers, tidal interactions, and AGN feedback, which are discussed in Section 1.2.1, all of which can either heat the ISM, preventing H₂ formation, or triggering a short burst of star formation, quickly exhausting H₂ supplies.

Conversely, rejuvenating galaxies show high H₂ to HI fractions, particularly at the low stellar mass end. This could indicate that high gas-phase metallicities are responsible for the efficient cooling of gas, allowing for HI to convert more easily to H₂. Or, since rejuvenating galaxies have more prominent bulges on average, they have deeper potential wells, allowing for higher density regions, thereby enabling for more efficient conversion of HI to H₂.

4. For low stellar masses, rejuvenating galaxies have high gas-phase metallicity compared to normal star-forming galaxies (Figure 3.16).

Galaxies without good emission line measurements do not have robust gas-phase metallicity measurements, so we do not plot the quenching or quenched galaxies, as, by definition, they have weak $H\alpha$ emission. Therefore, we cannot compare the quenching galaxies to a control population.

For matched SFR and stellar mass, we find that rejuvenating galaxies have higher gas-phase metallicities than star-forming galaxies at low stellar masses, which could explain the high H_2 abundances seen in the rejuvenating population. However, at the high stellar mass end, rejuvenating galaxies are poorly sampled, and we cannot draw any robust conclusions from this data. Rejuvenating galaxies with low SFR at the high stellar mass end likely have higher gas-phase metallicities, pushing their distribution above the star-forming population.

This trend also holds for the xCOLD GASS sample, although a significant fraction of metallicity measurements for rejuvenating galaxies are missing in this data set, so we cannot draw robust conclusions. However, the missing rejuvenating galaxies likely have metallicities that are higher than star-forming, as they have poor emission line measurements. This means that they likely have low SFRs, and, therefore, high gas-phase metallicities, which would be in line with the rest of the population.

Future Work

1. Resolved Spectroscopy

This thesis focused on global galaxy properties, where we are essentially averaging all features in a galaxy. This prevents us from detecting anomalies

in their stellar populations, and all spatial information is lost. Using resolved spectroscopy, we can study the star formation morphology of a galaxy and search for morphological differences between rejuvenating galaxies and the control star-forming population. Using the Mapping of Nearby Galaxies at Apache Point Observatory (MaNGA) survey (Bundy et al., 2015), we have access to resolved star formation maps, which provide visual insight into the possible mechanisms driving rejuvenation, as we can see any disturbances and unusual features in the distributions.

Using global measurements, we need to filter out galaxies hosting an AGN, since their emission in $H\alpha$ can be confused for active star formation. With resolved spectroscopy, we can identify and remove the specific pixels in a galaxy that are AGN-dominated, enabling us to keep galaxies we would normally discard. This is important as AGN feedback is a potential driver of rejuvenation. MaNGA is ideal for this work as it has resolved spectroscopic measurements for $\sim 10,000$ nearby galaxies. Preliminary work shows that the rejuvenating population tends to experience centrally enhanced star formation, pointing towards major or minor mergers or accretion from the IGM being dominant rejuvenation mechanisms, as these mechanisms likely funnel star-forming gas to the centres of galaxies (Mayer, 2009).

2. Star-Formation Histories

Our method for selecting rejuvenating galaxies limits us to identifying galaxies currently undergoing a period of rejuvenation since we only have one timescale available. With modern SED fitting routines (Robotham et al., 2020; Johnson et al., 2021), it is possible to reconstruct the star formation history for a galaxy

sample if sufficient multi-wavelength data is available. Past SED fitting codes have assumed a monotonic decrease in star formation rate since its first star formation event, which does not allow rejuvenation events. More recent SED fitting codes, such as ProSpect (Robotham et al., 2020), use a piecewise model instead. This permits the possibility of more than one-star formation event.

Previous studies have only tested piecewise SED fitting routines on small numbers of galaxies (Tanaka et al., 2023; Zhang et al., 2023); we can extend this work by applying the technique to a statistical sample of galaxies to search for trends in the star formation histories that are unique to the rejuvenating population. This will allow us to expand our sample by detecting both currently rejuvenating galaxies and galaxies that have previously rejuvenated. With the star formation histories in hand, we can determine if rejuvenation is a recurring event and investigate trends in the star formation histories that are characteristic of rejuvenating galaxies. This work will give insight into how common rejuvenation events are and reveal if rejuvenation is a recurring phenomenon in a galaxy’s life cycle.

3. Simulations

Our current understanding of rejuvenating galaxies is drawn from observational data with spatial and temporal resolution limitations. We are restricted to observing the galaxy at only one point in its lifetime and must extrapolate backwards using techniques such as observing at different wavelengths and SED fitting. With these methods, we are confined to coarse timesteps, losing critical information about the galaxy’s detailed evolution.

With simulations, we can watch a galaxy evolve with high temporal resolution and uncover the mechanisms by which they rejuvenate. We can also determine if rejuvenation events are common throughout a galaxy’s history. The possible mechanisms driving rejuvenation, including accretion, AGN feedback, mergers, or other internal processes, can be directly observed, constrained, and measured in simulations. Previous studies have been able to identify rejuvenating galaxies in simulations (Behroozi et al., 2019; Springel et al., 2018; Zhang et al., 2021), but none have studied how they rejuvenate.

We can fill in this gap by identifying rejuvenating galaxies in modern hydrodynamical simulations and searching for properties that distinguish rejuvenating and rejuvenated galaxies from a typical star-forming population. We can also observe individual galaxies throughout their lifetimes to determine the processes causing rejuvenation. We can use multiple galaxy evolution simulations like IllustrisTNG (Nelson et al., 2018), EAGLE (Crain et al., 2015), and Gasoline (Wadsley et al., 2017), which all use different assumptions and star formation prescriptions, to ensure robust findings.

Bibliography

Abazajian K. N., et al., 2009, ApJS, 182, 543

Accurso G., et al., 2017, MNRAS, 470, 4750

Akhshik M., et al., 2021, ApJ, 907, L8

Antonucci R., 1993, ARA&A, 31, 473

Baker W. M., Maiolino R., Bluck A. F. L., Lin L., Ellison S. L., Belfiore F., Pan H.-A., Thorp M., 2022, MNRAS, 510, 3622

Baldry I. K., Glazebrook K., Brinkmann J., Ivezić Ž., Lupton R. H., Nichol R. C., Szalay A. S., 2004, ApJ, 600, 681

Baldwin J. A., Phillips M. M., Terlevich R., 1981, PASP, 93, 5

Balsara D., Livio M., O’Dea C. P., 1994, ApJ, 437, 83

Behroozi P., Wechsler R. H., Hearin A. P., Conroy C., 2019, MNRAS, 488, 3143

Bell E. F., Baugh C. M., Cole S., Frenk C. S., Lacey C. G., 2003, MNRAS, 343, 367

Blanton M. R., Kazin E., Muna D., Weaver B. A., Price-Whelan A., 2011a, AJ, 142, 31

Blanton M. R., Kazin E., Muna D., Weaver B. A., Price-Whelan A., 2011b, AJ, 142, 31

Bolatto A. D., et al., 2017, ApJ, 846, 159

- Boselli A., Cortese L., Boquien M., Boissier S., Catinella B., Lagos C., Saintonge A., 2014, *A&A*, 564, A66
- Brinchmann J., Charlot S., White S. D. M., Tremonti C., Kauffmann G., Heckman T., Brinkmann J., 2004, *MNRAS*, 351, 1151
- Bromm V., Ferrara A., Coppi P. S., Larson R. B., 2001, *MNRAS*, 328, 969
- Brown T., Catinella B., Cortese L., Kilborn V., Haynes M. P., Giovanelli R., 2015, *MNRAS*, 452, 2479
- Brown T., Cortese L., Catinella B., Kilborn V., 2018, *MNRAS*, 473, 1868
- Brown T., et al., 2021, *ApJS*, 257, 21
- Bundy K., et al., 2015, *ApJ*, 798, 7
- Burgarella D., Buat V., Iglesias-Páramo J., 2005, *MNRAS*, 360, 1413
- Calette A. R., Avila-Reese V., Rodríguez-Puebla A., Hernández-Toledo H., Papastergis E., 2018, *Rev. Mexicana Astron. Astrofis.*, 54, 443
- Cano-Díaz M., Ávila-Reese V., Sánchez S. F., Hernández-Toledo H. M., Rodríguez-Puebla A., Boquien M., Ibarra-Medel H., 2019, *MNRAS*, 488, 3929
- Cappellari M., et al., 2011, *MNRAS*, 413, 813
- Carroll B. W., Ostlie D. A., 2017, *An introduction to modern astrophysics*, Second Edition
- Catinella B., et al., 2010, *MNRAS*, 403, 683

Catinella B., et al., 2018, MNRAS, 476, 875

Cleland C., McGee S. L., 2020, Monthly Notices of the Royal Astronomical Society, 500, 590

Cluver M. E., Jarrett T. H., Dale D. A., Smith J. D. T., August T., Brown M. J. I., 2017, ApJ, 850, 68

Conselice C. J., 2006, MNRAS, 373, 1389

Conselice C. J., 2021, in , Galaxies: Formation and Evolution. pp 181–208

Crain R. A., et al., 2015, MNRAS, 450, 1937

Cutri R. M., et al., 2013, Explanatory Supplement to the AllWISE Data Release Products, Explanatory Supplement to the AllWISE Data Release Products, by R. M. Cutri et al.

De Vis P., et al., 2019, A&A, 623, A5

Díaz-García S., Knapen J. H., 2020, A&A, 635, A197

Djorgovski S., Davis M., 1987, ApJ, 313, 59

Dou J., et al., 2021, ApJ, 907, 114

Durbala A., Finn R. A., Crone Odekon M., Haynes M. P., Koopmann R. A., O'Donoghue A. A., 2020, AJ, 160, 271

Evans F. A., Parker L. C., Roberts I. D., 2018, MNRAS, 476, 5284

Faber S. M., Gallagher J. S., 1979, ARA&A, 17, 135

Freeman K. C., 1970, ApJ, 160, 811

Fujita Y., 1998, ApJ, 509, 587

Giovanelli R., et al., 2005, The Astronomical Journal, 130, 2598

Gobat R., Magdis G., D'Eugenio C., Valentino F., 2020, A&A, 644, L7

Graham A. W., Worley C. C., 2008, MNRAS, 388, 1708

Groves B., 2007, in Ho L. C., Wang J. W., eds, Astronomical Society of the Pacific Conference Series Vol. 373, The Central Engine of Active Galactic Nuclei. p. 511 ([arXiv:astro-ph/0612309](https://arxiv.org/abs/astro-ph/0612309)), doi:10.48550/arXiv.astro-ph/0612309

Guo H., Jones M. G., Wang J., Lin L., 2021, ApJ, 918, 53

Hao C.-N., Kennicutt R. C., Johnson B. D., Calzetti D., Dale D. A., Moustakas J., 2011, ApJ, 741, 124

Hopkins P. F., Hernquist L., Cox T. J., Kereš D., 2008, ApJS, 175, 356

Huang M.-L., Kauffmann G., 2014, MNRAS, 443, 1329

Huang S., Haynes M. P., Giovanelli R., Brinchmann J., 2012, ApJ, 756, 113

Hubble E. P., 1926, ApJ, 64, 321

Hubble E. P., 1936, Realm of the Nebulae

Hudson M. J., et al., 2015, MNRAS, 447, 298

Iben Icko J., 1967, ARA&A, 5, 571

Ishibashi W., Fabian A. C., 2012, MNRAS, 427, 2998

- Israel F., 2000, in Combes F., Pineau Des Forets G., eds, *Molecular Hydrogen in Space*. p. 293 ([arXiv:astro-ph/0001250](https://arxiv.org/abs/astro-ph/0001250)), doi:10.48550/arXiv.astro-ph/0001250
- Jiménez-Donaire M. J., et al., 2019, *ApJ*, 880, 127
- Johnson B. D., Leja J., Conroy C., Speagle J. S., 2021, *ApJS*, 254, 22
- Jones A. P., Nuth J. A., 2011, *A&A*, 530, A44
- Kashino D., et al., 2013, *ApJ*, 777, L8
- Kauffmann G., et al., 2003a, *MNRAS*, 341, 54
- Kauffmann G., et al., 2003b, *MNRAS*, 346, 1055
- Kennicutt Robert C. J., 1998a, *ARA&A*, 36, 189
- Kennicutt Robert C. J., 1998b, *ApJ*, 498, 541
- Kewley L. J., Dopita M. A., Sutherland R. S., Heisler C. A., Trevena J., 2001, *ApJ*, 556, 121
- Khostovan A. A., et al., 2021, *MNRAS*, 503, 5115
- Kormendy J., Ho L. C., 2013, *ARA&A*, 51, 511
- Kormendy J., Richstone D., 1995, *ARA&A*, 33, 581
- Kormendy J., Fisher D. B., Cornell M. E., Bender R., 2009, *ApJS*, 182, 216
- Lambas D. G., Alonso S., Mesa V., O’Mill A. L., 2012, *A&A*, 539, A45
- Leroy A. K., et al., 2009, *AJ*, 137, 4670

- Lower S., Narayanan D., Leja J., Johnson B. D., Conroy C., Davé R., 2020, ApJ, 904, 33
- Ludwig R. R., Greene J. E., Barth A. J., Ho L. C., 2012, ApJ, 756, 51
- Mannucci F., Cresci G., Maiolino R., Marconi A., Gnerucci A., 2010, MNRAS, 408, 2115
- Marino R. A., et al., 2013, A&A, 559, A114
- Martig M., Bournaud F., Teyssier R., Dekel A., 2009, ApJ, 707, 250
- Martín-Navarro I., Shankar F., Mezcua M., 2022, MNRAS, 513, L10
- Martin D. C., et al., 2005, ApJ, 619, L1
- Mayer L., 2009, in APS April Meeting Abstracts. APS Meeting Abstracts. p. J4.001
- McGaugh S. S., de Blok W. J. G., 1997, ApJ, 481, 689
- McMillan P. J., 2011, MNRAS, 414, 2446
- Meyer B. S., Zimmer E., 2006, in Lauretta D. S., McSween H. Y., eds, , Meteorites and the Early Solar System II. p. 69
- Meynet G., Maeder A., 2003, A&A, 404, 975
- Moore B., Lake G., Katz N., 1998, ApJ, 495, 139
- Moorthy B. K., Holtzman J. A., 2006, MNRAS, 371, 583
- Narayanan D., Hopkins P. F., 2013, MNRAS, 433, 1223

Nelson D., et al., 2018, MNRAS, 475, 624

Nelson D., et al., 2019, Computational Astrophysics and Cosmology, 6, 2

Nersesian A., et al., 2019, A&A, 624, A80

Noll S., Burgarella D., Giovannoli E., Buat V., Marcillac D., Muñoz-Mateos J. C., 2009, A&A, 507, 1793

Obreschkow D., Rawlings S., 2009, MNRAS, 394, 1857

Omukai K., 2000, ApJ, 534, 809

Peng Y.-j., et al., 2010, ApJ, 721, 193

Peng Y., Maiolino R., Cochrane R., 2015, Nature, 521, 192

Peterson B. M., 2006, in Alloin D., ed., , Vol. 693, Physics of Active Galactic Nuclei at all Scales. p. 77, doi:10.1007/3-540-34621-X`3

Puglisi A., et al., 2016, A&A, 586, A83

Putman M. E., Grcevich J., Peek J. E. G., 2008, in Funes J. G., Corsini E. M., eds, Astronomical Society of the Pacific Conference Series Vol. 396, Formation and Evolution of Galaxy Disks. p. 233 (arXiv:0803.3069), doi:10.48550/arXiv.0803.3069

Quilis V., Moore B., Bower R., 2000, Science, 288, 1617

Ramón-Fox F. G., Aceves H., 2020, MNRAS, 491, 3908

Robotham A. S. G., Bellstedt S., Lagos C. d. P., Thorne J. E., Davies L. J., Driver S. P., Bravo M., 2020, MNRAS, 495, 905

- Roediger E., Hensler G., 2005, *A&A*, 433, 875
- Saintonge A., et al., 2011, *MNRAS*, 415, 32
- Saintonge A., et al., 2016, *MNRAS*, 462, 1749
- Saintonge A., et al., 2017, *ApJS*, 233, 22
- Saintonge A., et al., 2018, *MNRAS*, 481, 3497
- Salim S., et al., 2016, *ApJS*, 227, 2
- Sargent M. T., et al., 2014, *ApJ*, 793, 19
- Schawinski K., Thomas D., Sarzi M., Maraston C., Kaviraj S., Joo S.-J., Yi S. K., Silk J., 2007, *MNRAS*, 382, 1415
- Schinnerer E., et al., 2019, *The Messenger*, 177, 36
- Schulz S., Struck C., 2001, *MNRAS*, 328, 185
- Silva L., Granato G. L., Bressan A., Danese L., 1998, *ApJ*, 509, 103
- Spilker J. S., et al., 2022, *ApJ*, 936, L11
- Springel V., et al., 2018, *MNRAS*, 475, 676
- Springob C. M., Haynes M. P., Giovanelli R., Kent B. R., 2005, *ApJS*, 160, 149
- Stewart K. R., 2009, in Jogee S., Marinova I., Hao L., Blanc G. A., eds, *Astronomical Society of the Pacific Conference Series Vol. 419, Galaxy Evolution: Emerging Insights and Future Challenges*. p. 243 ([arXiv:0902.2214](https://arxiv.org/abs/0902.2214)), [doi:10.48550/arXiv.0902.2214](https://doi.org/10.48550/arXiv.0902.2214)

- Strauss M. A., et al., 2002, *AJ*, 124, 1810
- Tacconi L. J., et al., 2010, *Nature*, 463, 781
- Tanaka T. S., Shimasaku K., Tacchella S., Ando M., Ito K., Yesuf H. M., Matsui S., 2023, *PASJ*,
- Thomas D., Maraston C., Schawinski K., Sarzi M., Silk J., 2010, *MNRAS*, 404, 1775
- Tremonti C. A., et al., 2004, *ApJ*, 613, 898
- Trussler J., Maiolino R., Maraston C., Peng Y., Thomas D., Goddard D., Lian J., 2020, *MNRAS*, 491, 5406
- Valiante E., et al., 2016, *MNRAS*, 462, 3146
- Wadsley J. W., Keller B. W., Quinn T. R., 2017, *MNRAS*, 471, 2357
- Wakelam V., et al., 2017, *Molecular Astrophysics*, 9, 1
- Weidner C., Vink J. S., 2010, *A&A*, 524, A98
- Wetzel A. R., Tinker J. L., Conroy C., 2012, *MNRAS*, 424, 232
- Williams D. A., 2005, in *Journal of Physics Conference Series*. pp 1–17, doi:10.1088/1742-6596/6/1/001
- Wilson C. D., 1995, *ApJ*, 448, L97
- Wright E. L., et al., 2010, *AJ*, 140, 1868
- Wyse R. F. G., Gilmore G., Franx M., 1997, *ARA&A*, 35, 637

Zabel N., et al., 2019, MNRAS, 483, 2251

Zhang Z., et al., 2021, A&A, 650, A155

Zhang J., Li Y., Leja J., Whitaker K. E., Nersesian A., Bezanson R., van der
Wel A., 2023, ApJ, 952, 6